

Attribution-NonCommercial 4.0 International (CC BY-NC 4.0)

<https://creativecommons.org/licenses/by-nc/4.0/>

Access to this work was provided by the University of Maryland, Baltimore County (UMBC) ScholarWorks@UMBC digital repository on the Maryland Shared Open Access (MD-SOAR) platform.

**Please provide feedback**

Please support the ScholarWorks@UMBC repository by emailing [scholarworks-group@umbc.edu](mailto:scholarworks-group@umbc.edu) and telling us what having access to this work means to you and why it's important to you. Thank you.

# Earth and Space Science



## RESEARCH ARTICLE

10.1029/2022EA002767

### Key Points:

- A new approach simultaneously estimates water level and wave height using Global Navigation Satellite System observations in the Pacific high wave coastal environment
- Levels are determined with 9.4 cm error (RMS) and the astronomic tide (with a range over 2 m) is determined with 5.9 cm error, with respect to a traditional gauge
- Given a short calibration, significant wave height achieves an RMS error of 15 cm compared to a traditional gauge

### Supporting Information:

Supporting Information may be found in the online version of this article.

### Correspondence to:

I. Sepúlveda,  
[isepulveda@sdsu.edu](mailto:isepulveda@sdsu.edu)

### Citation:

Sepúlveda, I., Cao, B., Haase, J. S., & Murphy, M. J. Jr. (2023). Optimizing simultaneous water level and wave measurements from multi-GNSS interferometric reflectometry over 1 year at an exposed coastal site. *Earth and Space Science*, 10, e2022EA002767. <https://doi.org/10.1029/2022EA002767>

Received 29 NOV 2022

Accepted 2 JUN 2023

### Author Contributions:

**Conceptualization:** Ignacio Sepúlveda  
**Data curation:** Ignacio Sepúlveda, Bing Cao, Jennifer S. Haase  
**Formal analysis:** Ignacio Sepúlveda, Bing Cao, Jennifer S. Haase  
**Investigation:** Ignacio Sepúlveda, Bing Cao, Jennifer S. Haase, Michael J. Murphy Jr.  
**Methodology:** Ignacio Sepúlveda, Bing Cao, Jennifer S. Haase  
**Resources:** Jennifer S. Haase  
**Software:** Ignacio Sepúlveda, Bing Cao

© 2023 The Authors.

This is an open access article under the terms of the [Creative Commons Attribution-NonCommercial License](#), which permits use, distribution and reproduction in any medium, provided the original work is properly cited and is not used for commercial purposes.

## Optimizing Simultaneous Water Level and Wave Measurements From Multi-GNSS Interferometric Reflectometry Over 1 Year at an Exposed Coastal Site

Ignacio Sepúlveda<sup>1</sup> , Bing Cao<sup>2</sup> , Jennifer S. Haase<sup>2</sup> , and Michael J. Murphy Jr.<sup>2,3,4</sup> 

<sup>1</sup>Department of Civil, Construction and Environmental Engineering, San Diego State University, San Diego, CA, USA, <sup>2</sup>Institute of Geophysics and Planetary Physics, Scripps Institution of Oceanography, University of California San Diego, La Jolla, CA, USA, <sup>3</sup>Global Modeling and Assimilation Office, NASA, Greenbelt, MD, USA, <sup>4</sup>University of Maryland, Baltimore County/GESTAR-II, Baltimore, MD, USA

**Abstract** Global Navigation Satellite System Interferometric Reflectometry (GNSS-IR) measures water level using the interference pattern in signal-to-noise ratio (SNR) from direct and reflected signals off the sea surface, retrieved from standard geodetic antennas. Significant wave height is also measured by determining the satellite elevation angles where reflections become incoherent. We developed an approach for standard geodetic antennas to simultaneously measure sea levels and waves using a criterion for identifying coherent reflections. We tested the method at an exposed coastal environment at the E.B. Scripps Memorial Pier in California. The 1-year test captures a broad range of sea states and benefits from several co-located standard oceanographic sensors. By including GPS, Galileo, and GLONASS observations, the retrieval rate increases by a factor of  $\sim 2$  over GPS alone. Uncorrected water levels are estimated with a root-mean-square (RMS) error of 18.2 cm with respect to a conventional tide gauge. We further developed a simplified correction to remove the effect of phenomena altering the SNR oscillatory frequency and phase, which reduces RMS errors to 9.4 cm. We estimate the significant wave height with 15 cm RMS error with respect to a traditional wave gauge. The method, however, requires a short calibration. We find the wave height errors increase abruptly beyond a fixed limit when high waves are present, that may be a result of the particular deployment geometry. With this caveat, the technology could be useful to deploy in under-sampled regions affected by compounded coastal hazards, such as in areas affected by tropical cyclones and flooding.

**Plain Language Summary** Signals from Global Navigation Satellite Systems (GNSS), such as the Global Positioning System (GPS), that reflect off the ocean surface, when compared to signals that arrive directly at the antenna, reveal variations in signal strength that can be used to determine the elevation of the ocean surface. When the satellite elevation angle is too high above the horizon, the method to measure sea level no longer works. However, observing the elevation angle where this transition occurs allows us to measure the height of the waves that are preventing a strong reflected signal from being recorded. We develop criteria for obtaining the closest agreement between the GNSS-IR observations and the tide and wave gauge instruments on the Ellen Browning Scripps Memorial Pier in southern California over a 1 year period. Because it simultaneously measures changes in sea level and wave height, the method could be useful for measuring coastal hazards such as storm surge and flooding from hurricanes.

## 1. Introduction

### 1.1. Standard Observations of Coastal Water Level Variations

Long-term records of water levels and waves that describe the sea state in coastal areas are essential for urban planning and the design of coastal infrastructure. They capture measurements of extreme events, such as strong extratropical and tropical cyclones, that are necessary for probabilistic estimates of hazard and mitigation efforts. They also provide important ground-truth data for marine analyses, validation data for numerical forecasts, and useful information for environmental and marine energy assessments.

Because of their regularity, typical astronomic tidal variations on the order of 1–4 m of amplitude usually pose little hazard to urban infrastructure. Even large tides of up to 6 m (e.g., at Saint Malo, France and Chiloe Inland Sea, Chile) are usually not dangerous because construction has evolved to accommodate this range. Tides can

**Validation:** Ignacio Sepúlveda, Bing Cao, Jennifer S. Haase

**Visualization:** Ignacio Sepúlveda, Bing Cao, Michael J. Murphy Jr.

**Writing – original draft:** Ignacio Sepúlveda, Jennifer S. Haase, Michael J. Murphy Jr.

**Writing – review & editing:** Ignacio Sepúlveda, Bing Cao, Jennifer S. Haase

vary because of coastal bathymetry and local conditions, but because they are stationary, a few months of measurements are usually sufficient to determine astronomic tide constituents to predict local tide levels at any time (Pugh, 1987). Intermediate time scale observations of sea level (annual and interannual) could be useful for calibrating models in areas with large variations, including those affected by long term sea level rise or tectonic subsidence and uplift. Most importantly, when high tides are combined with other phenomena such as high storm surge, high waves, heavy precipitation and tsunamis, they can exacerbate coastal inundation hazards (Sepúlveda et al., 2022). The prediction of water level variations due to phenomena such as storm surge (Bernier & Thompson, 2015), tsunamis (Sepúlveda et al., 2017; Winckler et al., 2017), and meteotsunamis and seiches, commonly rely on shallow water wave models which need calibration. Tropical cyclones are also a key driver of the need for sea level observations at intermediate time scales because of great coastal impacts.

Ocean surface waves with periods shorter than a minute are not as easily predicted in time and space. They depend on both distant and local winds, which represent their own prediction challenge, and they are significantly affected by local bathymetry. Global coupled ocean-atmosphere numerical models are commonly used to determine offshore sea state conditions (e.g., Janssen & Bidlot 2018). Further numerical models and/or theoretical/empirical relations (e.g., Burcharth & Hughes, 2000; Goda, 2015; Kang et al., 2020) are then used to calculate shoaling and runup processes to estimate wave height and period at the coast. These models and theoretical/empirical relations assume that conditions are stationary and are commonly calibrated with wave climatology measured at the coast for at least a few months. A much longer time period is needed to capture the climatology of extreme events. In addition, with accelerating climate change, the storm and resultant wave climatology is not expected to remain stationary (Portner et al., 2019) and continuous calibration may be needed. There is thus a pressing need to improve the accuracy of water level and wave models, and that effort requires in situ measurements.

Traditional coastal tide gauges are based on acoustic and microwave radar measurements of the sea surface (Park et al., 2014) or subsurface pressure measurements. They are located on coastal structures such as pier piles and docks that are usually isolated from the open ocean, and operate continuously to produce a long time history. Waves are usually measured continuously by near-shore coastal buoys (Behrens et al., 2018), however selected locations such as the Ellen B. Scripps pier have a permanent wave gauge installation that relies on a subsurface digital pressure sensor. Movable wave gauges can also be deployed on the seafloor for short periods or for individual storms (e.g., Kennedy et al., 2010). Long-term records in isolated areas without coastal infrastructure are scarce and associated with high deployment and operational costs. Hence, there is an interest in developing additional technologies for measuring water levels and waves in remote areas, such as techniques based on ubiquitous signals from Global Navigation Satellite Systems (GNSS).

## 1.2. Water Level and Wave Height Measurements Using GNSS Antennas

GNSS constellations, such as GPS, GLONASS, Galileo and BeiDou, were originally designed for positioning, navigation, and timing applications. GNSS signals (radio waves) can also be used for remote sensing of the Earth surface, in a technique termed GNSS Reflectometry (GNSS-R). Two GNSS-R methods have been developed for measuring water level. One method is based on the phase delay between direct and reflected signals retrieved by two antennas facing upward and downward (Löfgren et al., 2011) and another is based on signal-to-noise ratio (SNR) variations caused by the interference pattern resulting from the superposition of direct and reflected signals received by the antenna (referred to as GNSS-IR for interferometric reflectometry) (Anderson, 2000; Larson, Ray, et al., 2013). An early study compared the two methods and found comparable agreement with a tide gauge (Larson, Löfgren, & Haas, 2013; Löfgren et al., 2011). The second method, investigated in this study and hereafter referred to as GNSS-IR, uses a single upward facing RHCP antenna to record measurements of SNR (a type of normalized reception strength) from satellites whose direct signals are contaminated with reflections; at low elevation angles, an oscillating signature is discernible in the SNR data (Anderson, 2000; Larson, Ray, et al., 2013). The periodicity of the oscillations is related to the additional distance the reflected signal has traveled. For reflections off a water surface, the height of the reflector beneath the known antenna height is thus a measurement of water level. Larson, Ray, et al. (2013); Roesler and Larson (2018) described the implementation of the GNSS-IR technique based on the Lomb-Scargle periodogram for spectral analysis. The retrieved frequency of the spectral peak relates the SNR to the vertical distance from the antenna to the reflecting surfaces, referred to as the reflector height and denoted as  $H_R$  herein.

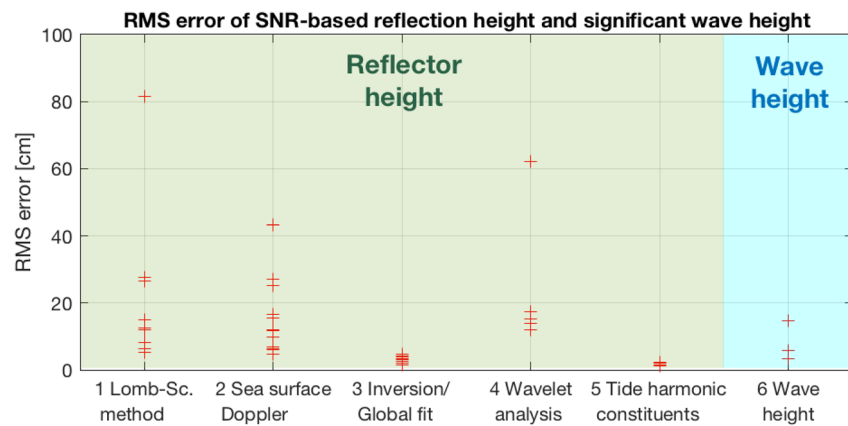


**Figure 1.** Summary of RMS errors in reflection height  $H_R$  (1–5) and significant wave height  $H_S$  (6) compiled from recent studies. We group the reported errors by calculation method and the type of result. We only compare results using the L1 band. We show the minimum error when different GNSS constellations or elevation angle ranges are analyzed. We excluded studies that used the classic Lomb-Scargle method with low-pass filtering of the  $H_R$  time series to reduce noise. One paper may report more than one error if it analyzes different locations. Values of Liu et al. (2017); Williams and Nievinski (2017); Tabibi et al. (2020); Strandberg et al. (2016) are also included in the inter-comparison study of Geremia-Nievinski et al. (2020).

The GNSS-IR method is susceptible to several sources of error when determining water levels, and previous studies have attempted to address them. Errors can be reduced by selecting a range of elevation and azimuthal angles that minimize the impact of reflections not originated from a uniform sea surface. These spurious reflections might cause either systematic errors, when originating from a large planar reflector, such as a sand beach; or random errors, when caused by smaller or more complex objects, such as nearby construction or trees. This leads to subjective decisions for data selection to eliminate problematic data. Data from some azimuths that do not have a clear view of the open ocean must be excluded, but even in the open ocean one study found that there was a particular azimuthal range that had to be eliminated due to large outliers (Larson et al., 2017). Other errors are related to the spectral analysis algorithm used for isolating the SNR oscillation frequency. The finite time duration (20–40 min) used in calculating the spectrum introduces errors if the water surface height is changing significantly over that period, which is usually the case when there are significant tides. Larson, Ray, et al. (2013) presented a correction to account for the temporally varying reflecting surface which we analyze later. Other studies have addressed the  $H_R$  measurement using more sophisticated inversion approaches. Nievinski and Larson (2014b); Strandberg et al. (2016, 2019) modeled the SNR signal using a decaying-amplitude (dampened) periodic function. The function is defined by a height-dependent frequency, phase offset and amplitude decay. They invert the SNR records by finding the best fitting function and then solving for a bias-free  $H_R$  value.

Because the noise in SNR time series depends on the roughness of the ocean surface, this can be exploited to retrieve information to measure waves. Specifically, the technique is able to measure the significant wave height, defined as the average of the trough to crest wave height of the highest 1/3 of the waves (Alonso-Arroyo et al., 2014; Goda, 2010), and which is denoted by  $H_S$  herein. By analyzing the persistence of coherent reflections as a function of the satellite elevation angle, Soulat et al. (2004); Alonso-Arroyo et al. (2014); Xin et al. (2008) demonstrated the feasibility of measuring  $H_S$  with several GNSS techniques (e.g., using one antenna configuration or a configuration consisting in a one upward and one downward looking antenna, plus a linearly polarized antenna pointing to the horizon). A technique close to GNSS-IR was first proposed by Alonso-Arroyo et al. (2014) using interference patterns in a single antenna configuration. Later, Roggenbuck et al. (2019) employed an approach based on the SNR amplitude decay to estimate wave height from a standard geodetic antenna.

### 1.3. Previous GNSS-IR Studies

Figure 1 presents the RMS  $H_R$  errors compiled from previous studies and classified according to the most commonly used calculation approaches. Group 1 (Liu et al., 2017; Löfgren et al., 2014; Peng et al., 2019; Puente & Valdés, 2019; Zheng et al., 2020) uses the standard approach based on the Lomb-Scargle periodogram alone. This approach is referred to as the standard procedure herein and is presented in Section 3 in detail. Group

2 (Larson et al., 2017; Larson, Löfgren, & Haas, 2013; Löfgren et al., 2014; Purnell et al., 2020; Strandberg et al., 2016; Williams & Nievinski, 2017) applies the Lomb-Scargle periodogram with the sea surface height-rate correction of Larson, Ray, et al. (2013). Group 3 (Puente & Valdés, 2019; Purnell et al., 2020; Strandberg et al., 2016, 2019; Tabibi et al., 2020) uses an SNR model and inversion method, as explained above. The method of Group 4 (Wang et al., 2019, 2020) is similar to that of Group 1 in the sense that it determines the interference oscillation period. This group, however, uses a wavelet analysis of the SNR signal instead of the Lomb-Scargle periodogram, which captures the temporal evolution of the SNR oscillation. This method has an accuracy comparable to that of Groups 1 and 2 but lower than that achieved by Group 3.

Group 3 estimates  $H_R$  with the highest accuracy. While the standard procedure of Group 1 is the simplest one, there is a large variation in reported accuracy. This may indicate that the procedure accuracy is sensitive to environment-specific local sea surface and atmospheric conditions, in addition to the calculation method. Indeed, Geremia-Nievinski et al. (2020) indicated that the higher accuracy achieved in their study (among the lowest errors for groups 1 and 3 in Figure 1) may be due to calm marine conditions in that location. The ocean surface wavefield plays a significant role in the accuracy of reflection height estimates. Rougher sea surfaces scatter the reflected signals (Alonso-Arroyo et al., 2014) and limit the range of elevation angles that can be used. The lower troposphere also induces refractive bending in the signal ray and modifies the propagation speed, compared to that in a vacuum. While errors due to refractive bending of several tens of centimeters have been estimated (Nikolaidou et al., 2020a), they seem to only affect the absolute mean sea level, and it is treated as a systematic error. In previous studies, this systematic error is simply removed by subtracting the time-averaged water level over the experiment duration (e.g., Geremia-Nievinski et al., 2020). However, these errors may be relevant for long-term sea level change studies. Finally, errors can be simply associated with a sub-optimal antenna deployment, in terms of horizontal location (too far from the water), mean height (too low), and directional orientation (upright vs. side-looking). The combination of these different types of errors is likely responsible for the wide range of accuracy estimates for the same calculation approach.

Considerable effort has been made to determine whether existing coastal geodetic GNSS stations, which have been operated for many years, can be exploited as tide gauges to describe the astronomic tide accurately. GNSS-IR estimates of tidal coefficients have been compared with those derived from nearby traditional tide gauges in several studies (Geremia-Nievinski et al., 2020; Larson et al., 2017; Löfgren et al., 2014). Accuracy in the predicted tidal coefficients and daily averaged sea levels are shown in Group 5 (Geremia-Nievinski et al., 2020; Larson et al., 2017; Löfgren et al., 2014; Purnell et al., 2020) in Figure 1. RMS errors are commonly below 5 cm. The high accuracy seen in such studies is explained by the fact that determining the longer periods of the tidal harmonic constituents is insensitive to the high frequency character of the GNSS-IR measurement errors. While some discrepancies in diurnal constituents are found between GNSS-IR and traditional tide gauge records (Larson et al., 2017), they do not impact the accuracy of tidal predictions significantly.

Group 6 of Figure 1 presents the RMS errors in the determination of  $H_S$ . Alonso-Arroyo et al. (2014), for instance, measured significant wave heights smaller than 0.7 m with an error standard deviation of 5.7 cm. This potential usage of GNSS-IR has received little attention, partly because the initial experiments used non-standard linearly polarized H-V antennas and complicated instrumentation that does not take advantage of the ubiquitous and simple to operate off-the-shelf GNSS technology that is currently available.

In this study, the first goal is to optimize the GNSS-IR technique so it is less susceptible to different sources of noise, in particular non-coherent reflections due to ocean roughness, by establishing objective criteria for determining the range of elevation angles to be used for water level measurements. We also aim to exploit more information from the SNR time series to improve its accuracy. The second goal is to develop an approach for using the transition from coherent to non-coherent reflections to retrieve  $H_S$  from the same standard GNSS antenna/receiver. We revisit the site of one of the first GNSS reflection experiments (Anderson, 2000), with new techniques and new multi-GNSS technology. The study benefits from the high quality and independent measurements on the Ellen Browning Scripps Memorial Pier at Scripps Institution of Oceanography in La Jolla, CA, to assess the accuracy of both  $H_R$  and  $H_S$  simultaneously. We compare our  $H_R$  and  $H_S$  measurements with a tide gauge operated by the National Oceanic and Atmospheric Administration (NOAA) and a wave gauge operated by the Scripps Institution of Oceanography Coastal Data Information Program (CDIP). Absolute height comparisons are also possible by the adoption of a common geodetic reference frame. Section 2 describes the experiment deployment. Section 3 improves the determination of  $H_R$  by introducing a criterion to identify the elevation angle



in which reflected GNSS rays transition from coherent to incoherent. In Section 4, GNSS  $H_R$  estimates are used to determine astronomic tidal constituents and residuals. Section 5 proposes a post-processing method which uses the SNR oscillation phase to reduce  $H_R$  errors. Section 6 proposes a calibration procedure to estimate the GNSS  $H_S$ . Finally, Section 7 discusses the study.

The derived GNSS-IR measurements of  $H_R$  and  $H_S$  are not as precise as traditional tide and wave gauges. The objective is to make a clear case for the utility of the lower accuracy measurements, given their accuracy at different temporal scales, when infrastructure is not available to support deploying traditional instruments.

## 2. Experimental 1-Year Deployment at Ellen Browning Scripps Memorial Pier

The GNSS antenna was installed at the end of the Ellen Browning Scripps Memorial Pier, in La Jolla, California. We used an Ashtech choke ring RHCP multi-GNSS antenna (model #: ASH701945.02B) that captures the GPS, GLONASS and Galileo frequency bands. For the initial part of the deployment (before 2 July 2020), we used a development kit with a Septentrio AsteRx4 OEM board. The latter part (after 2 July 2020) used a customized-built receiver with the same board. The AsteRx4 board has the capability of tracking multiple GNSS constellations and frequencies. A plastic radome (UNAVCO identifier: tall SCIGN) was installed on the antenna on 13 July 2020, which does not change the antenna phase center significantly within the scope of this experiment. We converted the raw observables measured by the receiver to standard RINEX format using the *teqc* code (Estey & Meertens, 1999). We extracted the SNR of each line-of-sight for  $L1$  (GPS and GLONASS) and  $E1$  Galileo measurements (all of them referred to as  $L1$  herein) using the code provided by Roesler and Larson (2018) (available at <https://github.com/kristinemlarson/gnssSNR>). This code also determines the appropriate satellite elevation angle and azimuth for each SNR observation using the satellite orbit and clock information obtained from GNSS ephemerides in SP3 files from the NASA Archive of Space Geodesy Data. The signal strength values are converted from  $C/N_0$  (in dB-Hz) to SNR (in W/W) using the conversion  $10^{C/N_0[dB-Hz]-Hz/10}$  (Strandberg, 2020). Although the standard choke ring antenna is designed to reduce multipath reflections, the reflected signal from the sea surface is sufficiently strong to create interference patterns in SNR records for elevation angles as low as  $1^\circ$ . The antenna is mounted so that it is pointed to zenith on a metallic boom at the northwestern corner of the pier oriented  $345^\circ$  with respect to north (see Figures 2a and 2b). We only use satellites at azimuths greater than  $200^\circ$ , to avoid spurious reflections from the pier structure to the southwest, and less than  $330^\circ$  so the antenna has a clear view to the sea surface from the range of satellite azimuths available given the orbital inclinations. Figure 2c shows the range of the reflection point locations for each satellite over the first day of deployment, representing the footprint centroid. The absolute height of the antenna was determined using GNSS precise point positioning (PPP) in the International Terrestrial Reference Frame (ITRF). The height was also related to the mean sea level (MSL) by using the NOAA leveling at the LAJO tide station. The official datum of the tide station (i.e., NAVD88) is related to the ITRF and the local MSL. The antenna (at antenna reference point, ARP) is located 11.12 m above MSL. A description of the antenna position in the local reference frame is presented in Table S1 and Figure S1 of the Supporting Information S1.

The sample rate for the GNSS receiver is 1 Hz. As we discuss below, this sample rate is sufficient to capture SNR oscillations and to determine  $H_R$  and  $H_S$  for an antenna  $\sim 10$  m above the sea surface. SNR time series of satellites arcs with minimum elevation angle as low as  $1^\circ$  with a duration longer than 10 min are stored for analysis. SNR data corresponding to elevation angles higher than  $30^\circ$  are disregarded because the amplitude of any periodic SNR oscillations in the observations is well below the background noise level. The final elevation angle ranges for the calculation of  $H_R$  and  $H_S$ , though, are further reduced based on the transition from coherent to incoherent reflection, described later in this paper. The receiver was shut down for half a day on March 2nd and between August 4th and 7th for maintenance. Figure 2g shows the sensing time duration for the first day of deployment.

## 3. Measurements of GNSS-IR Reflector Height ( $H_R$ )

The theoretical basis to determine  $H_R$  using GNSS-IR is explained here. We evaluate the  $H_R$  accuracy of the standard procedure and propose further improvements.

### 3.1. Method

As described by Georgiadou and Kleusberg (1988), the direct carrier signal can be simply modeled as a 1-D sinusoidal wave,  $S_D = A \cos(\Phi)$ , and the reflected signal as  $S_R = \alpha A \cos(\Phi + \Theta)$ . Here,  $A$  is the direct signal amplitude,

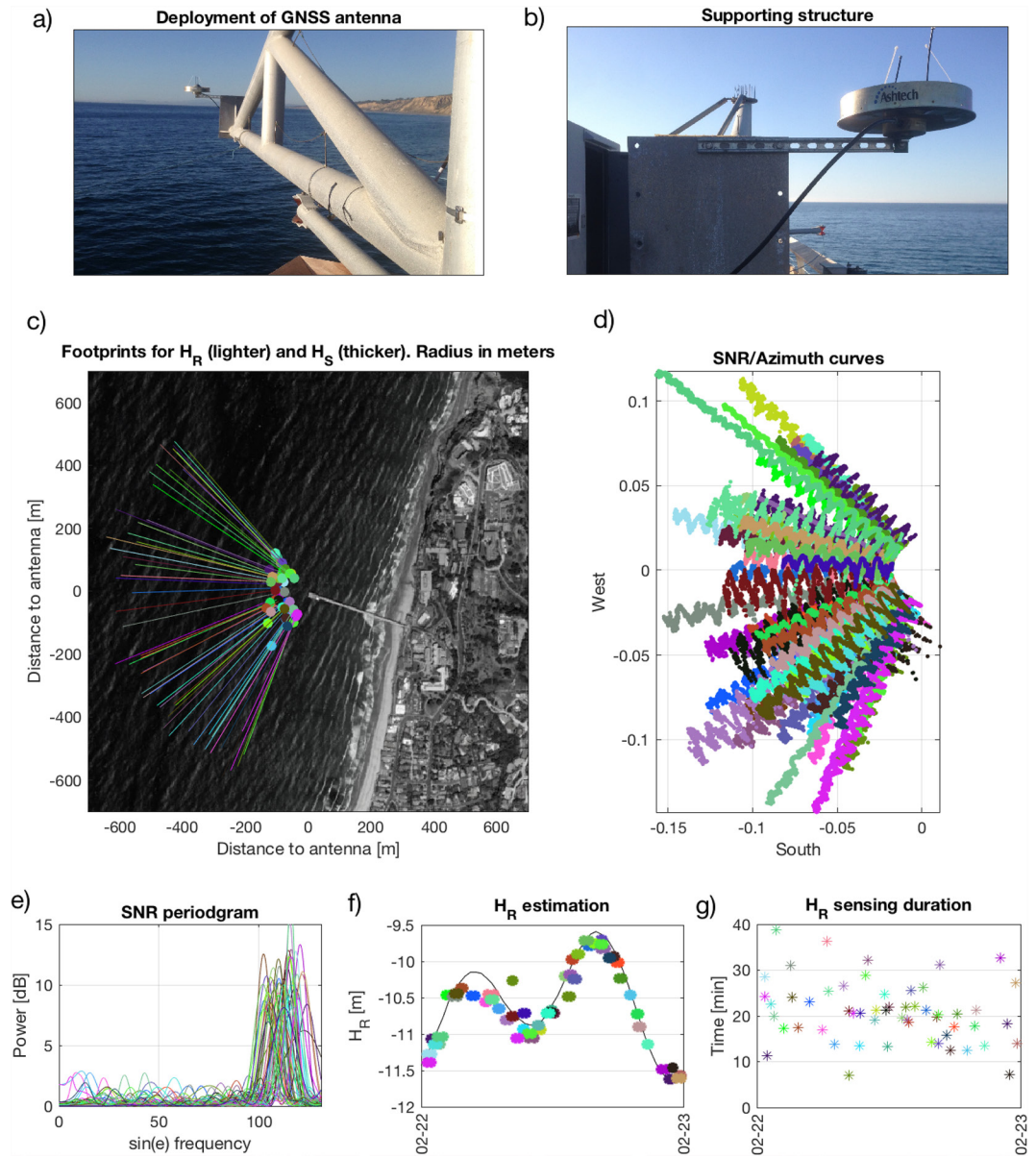


**Figure 2.** Experiment setup and observations from the first day of deployment. (a) Deployment on a metallic boom pointing to azimuth  $345^\circ$ . (b) Supporting structure. (c) Footprint centroid of the  $H_R$  calculation. The thin line represents the range of distance to the reflection over the sensing duration. The large dots indicate the specular point location where the reflection becomes incoherent and the significant wave height,  $H_S$ , is calculated. (d) SNR as a function of  $\sin(e)$  plotted at the corresponding azimuth. Low values of  $\sin(e)$  correspond to footprints farther from the antenna. (e) Lomb-Scargle power periodograms of the SNR time series normalized by the mean power over the resolved frequencies. (f) Estimated  $H_R$  over 1 day and comparison with the tide gauge record (black line). (g) Duration of SNR time series used for each  $H_R$  calculation. Each individual observation is represented by the same color in panels (c–g).

$\alpha$  is the attenuation factor of the reflected signal,  $\Phi$  is the carrier signal phase and  $\Theta$  is the geometric phase delay of the reflected signal (neglecting any non-geometric contributions from the sea surface permittivity, the antenna radiation pattern, tropospheric delays, etc), given by:

$$\Theta = 2\pi \frac{d}{\lambda}, \quad (1)$$

where  $d$  is the difference in traveled distance between the direct and reflected signals and  $\lambda$  are the GPS L1, GLONASS G1 and Galileo E1 wavelengths. The resulting signal due to interference at the antenna is given by,

$$S = S_D + S_R = \sqrt{1 + 2\alpha\cos(\Theta) + \alpha^2} \text{Acos} \left[ \Phi + \tan^{-1} \left( \frac{\sin(\Theta)}{\alpha^{-1} + \cos(\Theta)} \right) \right] \\ = \beta \text{Acos} \left[ \Phi + \left( \frac{\sin(\Theta)}{\alpha^{-1} + \cos(\Theta)} \right) \right], \quad (2)$$

where  $\beta$  is the time varying amplitude. The coefficient  $\alpha$  is a function of elevation angle and it depends on the roughness of the reflecting surface, on the sea surface salinity (via Fresnel reflection coefficients for a smooth surface), and on the antenna radiation pattern. For a grazing reflection on an RHCP antenna, the value of  $\alpha$  decreases with increasing elevation angle.

As far as GNSS-IR is concerned, we assume that the SNR is proportional to power or  $\beta^2$  so that,

$$SNR \sim \beta^2 = 1 + \alpha^2 + 2\alpha\cos(\Theta). \quad (3)$$

The term  $2\alpha\cos(\Theta)$  is periodic for variations of  $\Theta$ , which in turns depends on  $d$  and  $\lambda$ .  $d$  changes over the sensing duration while  $\lambda$  is fixed. Geometrically,  $d$  and the reflection height are related by,

$$d = 2H_R \sin(e), \quad (4)$$

where  $e$  is the elevation angle of the satellite measured from zero at the horizon. Substituting into Equation 1 gives

$$\Theta = \frac{4\pi H_R \sin(e)}{\lambda} = \omega \sin(e), \quad (5)$$

where  $\omega$  is the “frequency” of the periodic variation in units of  $1/\sin(e)$ .

Thus the interference oscillation frequency for the SNR time series when expressed as a function of  $\sin(e)$  can be used to determine the reflector height  $H_R$ . The SNR oscillation frequency can be determined by using a periodogram analysis and identifying the frequency of the most energetic spectral peak from the SNR record over the period when reflection is coherent. We denote this peak frequency as  $\omega_{\max}$ .

$$H_R = \omega_{\max} \frac{\lambda}{4\pi}. \quad (6)$$

Note that the known height of the antenna minus  $H_R$  constitutes a water level measurement. In this study we use the expressions  $H_R$  and water level interchangeably. We remove the global SNR trend by fitting a polynomial of degree 4 (Larson, Löfgren, & Haas, 2013). An example of de-trended SNR for the first day of deployment and rotated according to their azimuth is shown in Figure 2d, and examples for different GNSS constellations are shown in Figure 3. Larson, Ray, et al. (2013) proposed the use of the Lomb-Scargle periodogram for irregularly spaced data (Lomb, 1976) from de-trended SNR records over the period of time in which  $\Theta$  and  $e$  change. The variance-normalized power spectral densities of the Lomb-Scargle periodogram in terms of frequency  $\omega$  are given by (Scargle, 1982),

$$P(\omega) = \frac{1}{2\sigma^2} \left( \frac{[\sum_j (s_j - \bar{s}) \cos(\omega(t_j - \tau))]^2}{\sum_j \cos^2(\omega(t_j - \tau))} + \frac{[\sum_j (s_j - \bar{s}) \sin(\omega(t_j - \tau))]^2}{\sum_j \sin^2(\omega(t_j - \tau))} \right), \quad (7)$$

where the pairs  $(t_j, s_j)$  correspond to  $\sin(e)$  and SNR values of the  $j$ th observation, respectively,  $\sigma^2$  is the SNR variance,  $\bar{s}$  is the mean SNR value and  $\tau$  is the phase shift (in units of cycles) given by  $\tan(2\omega\tau) = \frac{\sum_j \sin(2\omega t_j)}{\sum_j \cos(2\omega t_j)}$ . Several existing algorithms can be used to compute the Lomb-Scargle periodogram (e.g., Press et al., 1992). Further details of the Lomb-Scargle periodogram are presented in Supporting Information S1. An example of the Lomb-Scargle periodograms for the first day of the deployment is shown in Figure 2e with the corresponding reflection heights,  $H_R$ , in Figure 2f.

The minimum sample rate capturing the SNR oscillation must be greater than the Nyquist frequency in time,

$$f_{\text{sample}} > f_{\text{Nyquist}} = \frac{2\omega_{\max}}{2\pi} \max \left[ \frac{d\sin(e)}{dt} \right] \quad (8)$$



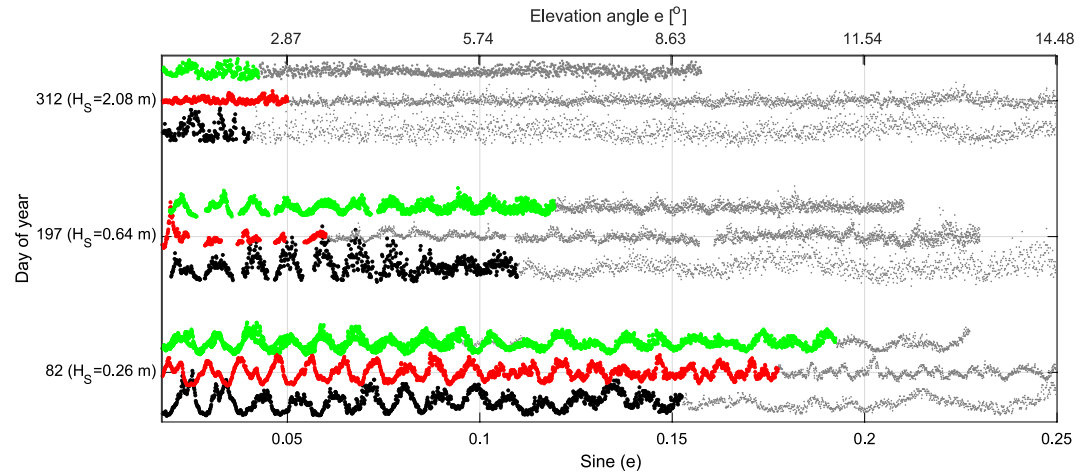


**Figure 3.** SNR records from GPS (black), GLONASS (red) and Galileo (green) satellites on March 22 (doy 82), July 15 (doy 197) and November 7 (doy 312) in 2020. Doy 312 corresponds to one of the days with the highest waves (i.e., a storm). The daily average significant wave heights are shown on the vertical axis legend. The gray dots show measurements in which reflections are not coherent, based on the coherent reflection criterion  $\Omega_c = 0.5$ , defined in Equation 10.

For  $H_R = 10$  m, and for  $L1$  (GPS) wavelengths, we have,

$$\frac{4H_R}{\lambda} \max \left[ \frac{d \sin(e)}{dt} \right] \approx \frac{4 \cdot 10 (1.4 \times 10^{-4})}{0.1905} \approx \frac{1}{34} \text{ Hz}, \quad (9)$$

which correspond to elevation angle change rates of  $0.0085^\circ/\text{s}$ . The sample rate of 1 Hz is well above the requirement.

### 3.2. Improvement Using a Coherent Reflection Criterion

For a given mean station height, the accuracy in determining  $H_R$  and  $\omega_{max}$  depends on the oscillation amplitude and noise of the SNR time series. With increasing elevation angle, the attenuation factor  $\alpha$  in Equation 2 becomes small so the SNR oscillation decreases in amplitude. This is seen in Figure 3 for the de-trended SNR record for day-of-year (doy) 82 with low wave conditions where the transition from incoherent to coherent reflections occurs between  $8^\circ$  and  $11^\circ$  elevation angle. The evolution from coherent to incoherent reflections depends on the sea surface roughness, which also reduces the amplitude and broadens the zone on the sea surface from which reflected energy returns. Thus the amplitude of the SNR oscillations decreases as sea surface roughness increases, and the transition from incoherent to coherent reflections occurs at lower elevation angles. Figure 3 shows de-trended SNR records for doys 82, 197 and 312 in 2020 which have different wave conditions for three GPS, Galileo, and GLONASS satellites. The highest waves occurred on doys 312 and the lowest ones on doys 82. The oscillation strength is preserved for larger elevation angles when waves are small. For the highest wave conditions, oscillations are only present for elevation angles smaller than  $3^\circ$ . Interferometric oscillations are strong for elevation angles as low as  $1^\circ$ . This illustrates that the duration of the oscillatory behavior depends on wave height.

We define a criterion to determine the elevation angle range in which reflections are coherent and interferometric oscillations are sufficiently strong. A similar idea was first proposed by Alonso-Arroyo et al. (2014) for wave height measurement purposes, in which the power of the de-trended SNR spectral peak is calculated for different elevation angle ranges using the Fourier Transform. Incoherent reflections are identified where the power of the de-trended SNR spectral peak is smaller than a selected threshold. In our criterion, though, we compare the power of the spectral peak normalized by the variance of different elevation angle ranges, as shown in Equation 7, with respect to the spectral peak at the lowest elevation angles of the record. First, we de-trend the SNR time series. Second, we discard SNR time series with more than one spectral peak, possibly linked to more than one reflection source (Strandberg, 2020). This is done by selecting SNR signals whose spectral power peak is more than five times the average power over the analyzed frequency band. We also disregard observations in which the available  $\sin(e)$  range is shorter than 0.03 (as required for the third step). Third, SNR data over sub-ranges of  $\sin(e)$  of

0.03 units are analyzed. This sub-range contains  $\sim 3$  oscillations for our average reflection height of  $\sim 10$  m, and would be different for antennas deployed at different heights. The sub-ranges overlap and are generated every  $0.0025 \sin(e)$  units along the de-trended SNR. For each sub-range, the Lomb-Scargle periodogram of Equation 7 is calculated and denoted by  $P(\omega)^j$  for the  $j$ th sub-range. The variance-normalized power spectral peak amplitude at  $\omega_{\max}^j$ ,  $P(\omega_{\max}^j)^j$ , is a measure of the significance of the interferometric oscillation relative to the SNR record variance in such sub-range. Thus,  $P(\omega_{\max}^j)$  can be used to determine which sub-ranges contain strong interferometric oscillations. The first sub-range (i.e.,  $j = 1$ , starting at  $e = 1^\circ$ ) is expected to contain the greatest oscillation amplitudes. The criterion we use classifies subranges with coherent reflections as those that satisfy:

$$\frac{P(\omega_{\max}^j)^j}{P(\omega_{\max}^1)^1} > \Omega_c, \quad (10)$$

within  $0.75\omega_{\max}^1 < \omega_{\max}^j < 1.25\omega_{\max}^1$ .  $\Omega_c$  is specified by the user. A sensitivity analysis of  $\Omega_c$  is presented in the supplemental material, finding that  $\Omega_c = 0.5$  provides the most accurate values of  $H_R$  in our experiment. The black, red and green signals in Figure 3 show ranges in which the defined criterion is fulfilled. The gray extensions, on the other hand, show where the criterion is not fulfilled and reflections are classified as incoherent. The elevation angle at which the transition occurs is defined as elevation angle cut-off,  $e_{co}$ , in this study. The coherent reflection criterion is used to determine the most reliable elevation angle ranges to compute  $H_R$  and, later, for estimating significant wave height. Further tests are necessary to check if the criterion is effective for other antenna types and configurations. The criterion parameters also need further validation for other conditions.

### 3.3. Resulting $H_R$ Sea Level Measurements at E.B. Scripps Pier

We compute values of  $H_R$  following Equation 1 within a range of elevation angles defined by the coherent reflection criterion. For days with high waves we estimate very short ranges of  $\sin(e)$  with coherent reflection. In such a case, we specify a longer range  $e = [1^\circ - 6^\circ]$ . Figure 4a shows the GNSS-IR  $H_R$  retrievals. GPS, GLONASS and Galileo constellations contribute to 44.5%, 29.6% and 25.9% of the retrievals, respectively. In total, 15,570 retrievals are obtained in 366 days, which corresponds to an average of roughly 1.8 observations per hour. The black histograms of Figures 4d and 4e also show the statistics of the sensing duration (i.e., the time required to retrieve a single  $H_R$  value) and the temporal gaps between each observation (i.e., the time between the end of the previous observation and the initiation of next one) corresponding to 56% of the deployment duration when using an azimuth range between  $200^\circ$  and  $330^\circ$ . A few gaps as long as 2 hr are found. The statistics show that water level variations with periods shorter than 1 hr may not be captured if they happen in a gap or if the sensing duration is long. This limitation, e.g., may be relevant for tsunami waves with periods shorter than 1 hr. However, it may be sufficient for longer period phenomena such as tides and storm surge. We illustrate the advantage of using three constellations by showing the statistics of GPS retrievals alone as red bars in Figures 4d and 4e. The distributions of sensing duration have a similar shape. The gaps, however, increase from 56% to 77% of the total time using the same azimuth range and it shows the importance of using more than one constellation in GNSS-IR. The temporal sampling characteristics here are quite good, given the wide azimuthal visibility. The method would have even better temporal sampling for sites with a wider azimuthal range that captured more setting/rising GNSS satellites.

The blue curves in Figures 4a and 4c represent the record of a traditional tide gauge located at the same pier at LAJO station, operated by NOAA. To avoid uncertainties in the absolute reference of the GNSS antenna relative to the tide gauge reference, the tide gauge curve has the mean removed, then the mean reflection height of the GNSS-IR observations is also subtracted.

The tide gauge sensor has an accuracy of millimeters and because the data are derived from microwave sensors rather than pressure sensors, the data are not expected to be affected by seasonal temperature perturbations (e.g., Larson et al., 2017). The data is retrieved from the NOAA Tides and Currents website (<https://co-ops.nos.noaa.gov>) with a sampling interval of 6 min. The tide gauge has smaller measurement errors than the GNSS-IR technique and, therefore, is considered the reference for the true water level in this study. Hence, the difference between the GNSS-IR retrievals and the tide gauge record is defined as the GNSS-IR  $H_R$  error and is presented in Figure 4b. We removed the average of the GNSS-IR and tide gauge records and, therefore, the error has a zero mean. The error standard deviation,  $\sigma_e$ , is 18.2 cm over the 366-day deployment. The separate GPS, GLONASS and Galileo constellation retrievals correspond to error standard deviations of 18.4, 18.6 and 17.3 cm, respectively. Figure 4f shows a histogram of the water level errors. The histogram is slightly asymmetric. To evaluate

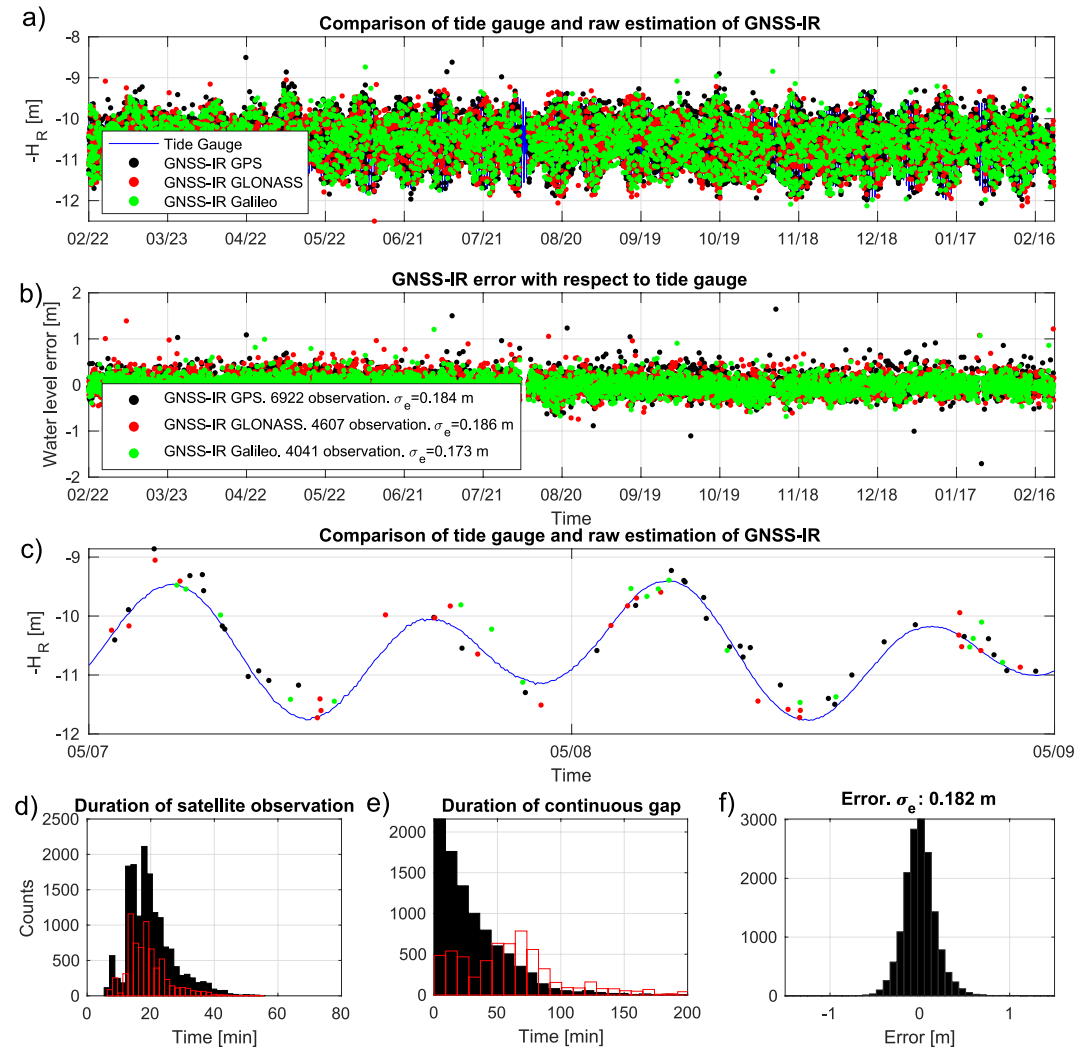


**Figure 4.** (a) Comparison of LAJO tide gauge (shifted) and reflection height  $H_R$  obtained with GNSS-IR without any corrections. On average, 43 measurements are obtained per day. (b) Water level measurement differences (GNSS-IR minus tide gauge). (c) GNSS-IR  $H_R$  and tide gauge (shifted) over 2 days of spring tides. (d) Sensing duration for the 15,570 retrievals (black) and GPS alone (red). (e) Distribution of the duration of temporal gaps for three-constellation GNSS (black) and GPS only (red). The total duration of time when no sensing is taking place reduces from 77% to 56% when using three constellations instead of GPS alone. (f) Distribution of  $H_R$  errors for the three constellations combined. The average water level from each time series is removed so errors have zero mean.

the effectiveness of the coherent reflection criterion, we compute  $H_R$  using a constant range from  $1^\circ$  to  $30^\circ$  for all the SNR time series. We obtain a lower accuracy corresponding to  $\sigma_e = 32.4$  cm. The fixed elevation angle range leads to not only larger errors but also to longer computational times.

#### 4. Measurements of Astronomic Tides Using GNSS-IR $H_R$

Many studies have tested the quality of existing GNSS-IR records for determining astronomic tide properties (e.g., Larson et al., 2017; Löfgren et al., 2011, 2014; Tabibi et al., 2020). If the astronomic tide is the dominant mechanism of water level variations, water levels can be predicted at any time via the determination of tidal harmonic constituents. We employ the GNSS-IR  $H_R$  measurements to determine these constituents.

##### 4.1. Astronomic Tide Constituents

We use the UTide code (Codiga, 2011) to estimate the tidal constituents from the unevenly time-spaced GNSS-IR observations using a least squares method. We adopt a Rayleigh criterion of 1.0 for the choice of main tidal

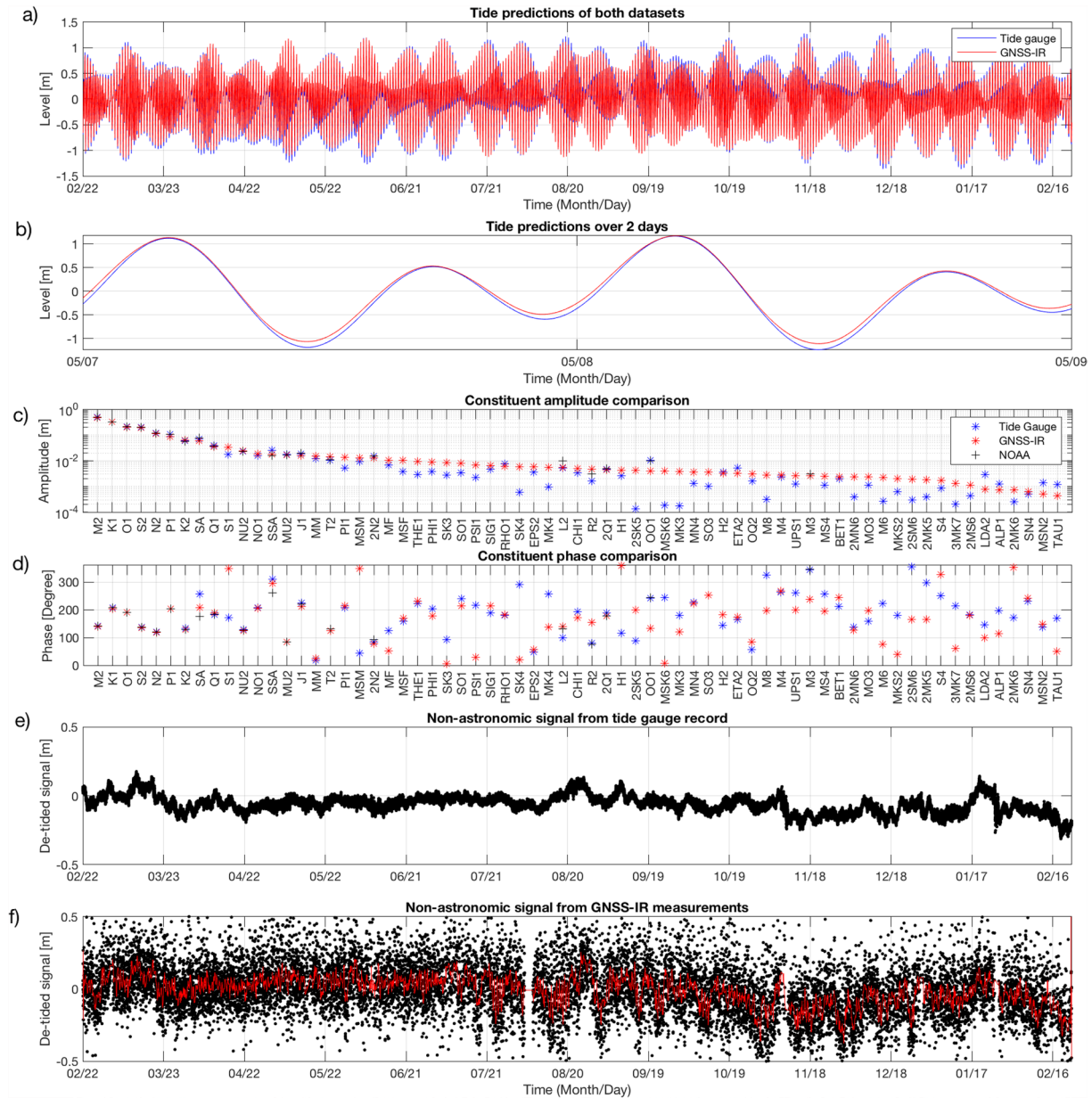


**Figure 5.** Tidal harmonic analysis derived from 1 year of tide gauge and GNSS-IR  $H_R$  measurements. (a) Tide predictions derived from 1 year of tide gauge data (blue) and 1 year of GNSS-IR  $H_R$  measurements using the method of Section 3.1 (red). The standard deviation of the difference between the two tide predictions is 5.9 cm. (b) Tide predictions over 2 days of spring tides. (c, d) Amplitude and phase of tidal constituents calculated from 1 year of tide gauge data (blue) and 1 year of GNSS-IR data (red), and the constituents reported by NOAA at LAJO station (black). (e) Residuals equal to the tide gauge observations minus predicted astronomic tide using the tide gauge observations. (f) Residuals equal to the GNSS-IR observations minus predicted astronomic tides using the GNSS-IR observations. The red curve corresponds to a 10 point median filtered version of the data.

constituents (Godin, 1970). For comparison, we also calculate the constituents using a 1 year record of the traditional tide gauge at LAJO station. Figures 5a and 5b show tide time histories constructed with the estimated tidal constituents. The standard deviation of the difference between astronomic tide predictions of the GNSS-IR and the tide gauge is 5.9 cm. To gain more insight about the quality of the constituent estimates, we plot an amplitude and phase comparison in Figures 5b and 5c. As a reference, we also present the constituents reported by NOAA at LAJO station. We observe small discrepancies for the first 9 dominant constituents that have amplitudes larger than 2 cm. For constituents with lower energy, significant discrepancies in amplitude and phase may be explained by the finite length of the records (1 year) and difficulties of the least squares method to isolate constituents with similar period (Codiga, 2011). Our results show that despite the standard deviation of  $\sigma_e$  is 18.2 cm for

the standard GNSS-IR procedure, it can determine astronomic tides with small discrepancies. This seems to be possible because GNSS-IR  $H_R$  errors tend to be higher frequency and the long period tidal constituents are less affected by them.

#### 4.2. Non-Tidal Residuals

We also analyze the non-tidal residuals of the tide gauge records. Figure 5e shows residuals where the tide prediction from the tide gauge is subtracted from the tide gauge observations. Figure 5f shows the GNSS-IR measurements minus the tide prediction from the very same GNSS-IR measurements. The residuals of the tide gauge record have small amplitudes, likely physical and associated with other low-frequency phenomena affecting water levels at the station such as internal waves and storm surge. The residuals of the GNSS-IR record are affected by stronger high-frequency noise not present in the tide gauge. The red curve in Figure 5f is a low-pass filtered version of the individual measurements. We obtain this curve by computing the median of ten consecutive retrievals (i.e., median in  $\sim 5$  hr). While the high-frequency noise is dominant in the GNSS-IR de-tided record, the red curve shows a low-frequency content similar to that of the tide gauge residuals. The amplitude of the low-frequency content varies along the year, having the lowest between April and July 2020. We use these residuals in the next section to further improve the accuracy of  $H_R$ .

### 5. Higher Order Empirical Corrections of $H_R$

The  $H_R$  estimation method of this study so far has only used the SNR oscillation frequency obtained from the Lomb-Scargle periodogram analysis (i.e.,  $\omega_{\max}$ ). Nievinski and Larson (2014a); Tabibi et al. (2017) proposed the use of more sophisticated functional forms to analyze SNR time series by means of a forward/inverse approach. These functional forms exploit not only  $\omega_{\max}$ , but also the changes (biases) in SNR oscillation amplitude and phase. These additional properties have been also exploited to determine the effective reflection depth in soil moisture studies (Larson, Small, Gutmann, Bilich, Axelrad, et al., 2008; Larson, Small, Gutmann, Bilich, Braun, et al., 2008). Here, we will exploit additional properties of the SNR oscillations to reduce  $H_R$  errors.

#### 5.1. Phase-Based Correction Method for $H_R$ Estimates

For water level measurements, Strandberg et al. (2019) proposed fitting a model to the SNR time series based on B-splines. This model implicitly includes the SNR amplitude and phase in the calculation. Tabibi et al. (2020) also provided an analytical study of the relation between the SNR phase bias and  $H_R$  errors. Here, we propose a simple correction strategy for the  $H_R$  standard procedure for increasing the accuracy and it is called herein the phase-based correction.

The parameter  $\beta^2$ , assumed to be proportional to the SNR, can be modeled as in Equation 3 and decomposed into two terms as follows,

$$\beta^2 = 1 + 2\alpha\cos(\Theta) + \alpha^2 \sim \overline{SNR} + SNR', \quad (11)$$

where  $\overline{SNR}$  is the long term trend and which is removed using a polynomial fit, as previously explained. The de-trended component is modeled as (Strandberg et al., 2019),

$$SNR' = Ce^{-D\sin^2(e)}\cos(\Theta + \Phi_{snr}). \quad (12)$$

where  $\Theta = \frac{4\pi H_R}{\lambda}\sin(e)$  as given by Equation 1,  $\Phi_{snr}$  is the SNR oscillation phase shift and  $Ce^{-D\sin^2(e)}$  is the SNR amplitude decay. We fit values of the parameters  $C$ ,  $D$ ,  $\Phi_{snr}$  and  $\omega_{\max} = \frac{d\Theta}{d\sin(e)}$  using the SNR time series as follows. First, we use the variance decay inferred from the variances of the SNR sub-ranges in Section 3.1 to find the parameter  $D$ . Second, we remove the amplitude modulation from the signal by dividing detrended SNR by the factor  $e^{-D\sin^2\theta}$ . Third, we use the Lomb-Scargle periodogram analysis of Equation 7 to find  $\omega_{\max} = \frac{d\Theta}{d\sin(e)}$ . Finally, we apply a Fourier expansion with one term to obtain  $C$  and  $\Phi_{snr}$ . We fit a cosine and sine function with frequency  $\omega_{\max}$  and coefficients  $a_c$  and  $b_s$ , respectively. The amplitude factor is obtained from  $C = \sqrt{a_c^2 + b_s^2}$ .  $\Phi_{snr}$  is given by  $\tan^{-1}(b_s/a_c)$ , with values between  $\pi$  and  $-\pi$ .

The new values of  $\omega_{\max}$  and corresponding  $H_R$ , after removing the factor  $e^{-D\sin^2\theta}$  from the de-trended SNR record, have nearly the same errors as those of the standard procedure in Section 3.1. The RMS error of  $H_R$  compared to



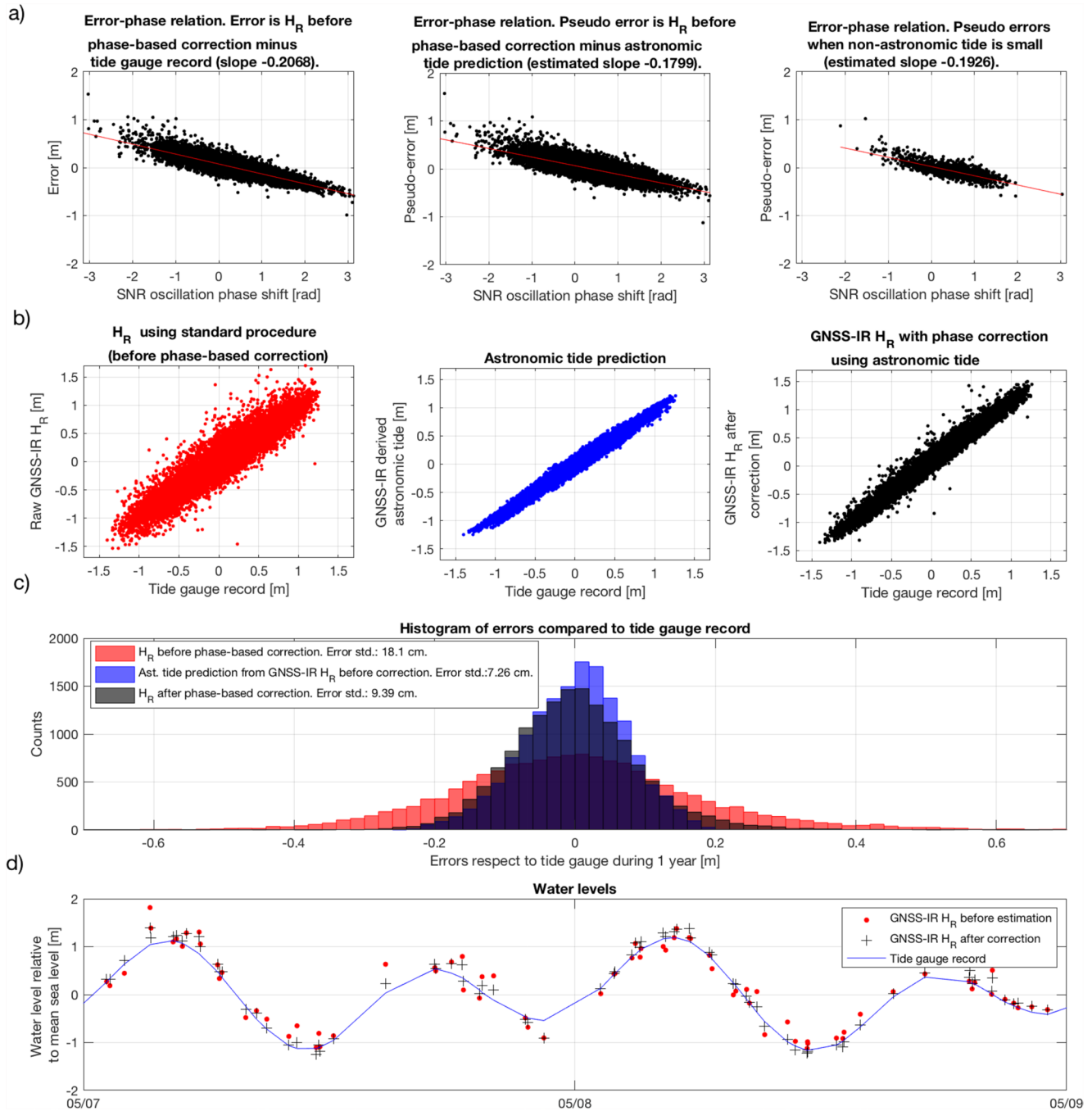


**Figure 6.** Accuracy of  $H_R$  using phase-based correction compared to other water level estimates. (a) Comparison of  $H_R$  error versus the phase shift of the SNR oscillation,  $\Phi_{snr}$ .  $H_R$  errors are the difference between  $H_R$  (before correction) minus the tide gauge record (left panel).  $H_R$  pseudo-errors are defined as  $H_R$  minus the astronomic tide prediction derived from GNSS-IR. Pseudo error scatter plots are presented for 1 year (middle panel) and 1 month where non-astronomic tides are small (right panel). (b) Comparison of the tide gauge record with  $H_R$  before phase-based correction (red dots), the astronomic tide prediction derived from GNSS-IR (blue) and  $H_R$  after phase-based correction (black crosses). (c) Histogram of differences with respect to the tide gauge record over 1 year. (d) Time series of the water level over 2 days for  $H_R$  before phase-based correction, the  $H_R$  after phase-based correction and the tide gauge record.

the tide gauge record slightly reduces from 18.2 to 18.1 cm. The phase shift  $\Phi_{snr}$  of Equation 11, though, provides further information about the errors in  $H_R$ . There is a strong correlation between the fitted  $\Phi_{snr}$  and the GNSS-IR  $H_R$  error, which is presented in Figure 6a (left panel). The scatter plot of  $H_R$  error versus  $\Phi_{snr}$  has a constant slope and crosses the origin. A few outliers are due to phase shifts greater than  $\pi$  or smaller than  $-\pi$ , which can be easily

identified and corrected. This relation between the calculated  $\Phi_{snr}$  and  $H_R$  error can be exploited to improve the GNSS-IR measurement accuracy.

## 5.2. Use of Derived Tides for Phase-Based Correction of $H_R$

Although the correlation between  $H_R$  errors and  $\Phi_{snr}$  is strong, the relation is unknown when independent accurate water level measurements are not available. After calculating  $H_R$  and  $\Phi_{snr}$  from the Lomb-Scargle periodogram analysis and the Fourier expansion, respectively, we propose an approximate and simplified correction using the astronomic tide analysis of Section 4.  $H_R$  records include astronomic and non-astronomic water level variations. The intensity and relevance of non-astronomic variations were evaluated by calculating the difference between the observations and the predicted tide based on the tidal coefficients, which we refer to as the non-tidal residuals. The low frequency content of the GNSS-IR residuals in Figure 5f, represented by the median low-pass filtered signal (red curve), is similar to the residuals of the tide gauge record in Figure 5e. An example of a period with small residuals and, therefore, small non-astronomic variations is the 30-day period between March 25 and April 25. During this period, the difference between the GNSS-IR  $H_R$  measurements and their corresponding GNSS-IR-based astronomic tide prediction serves as a pseudo-error from which the correlation-based correction can be determined. Figure 6a shows a comparison of  $\Phi_{snr}$  with errors and pseudo errors. The left panel shows the true error. The middle panel compares the pseudo errors for the entire experiment, and the right panel uses only the period between March 25 and April 25. The right panel has less dispersion than the middle panel and it has a slope closer to the actual true error-phase relation. The slope fitted with the pseudo-error is used to correct  $H_R$  values obtained with the Lomb-Scargle periodogram analysis. Figure 6b presents scatter plots of the tide gauge record versus  $H_R$  obtained with the standard procedure, the predicted astronomic tide and the phase-corrected  $H_R$  calibrated with pseudo-errors between March 25 and April 25.

## 5.3. Improved $H_R$ Measurements After Empirical Phase-Based Correction at E.B. Scripps Pier Using the SNR Oscillation Phase

Figure 6c also shows the error histograms for the entire year of GNSS-IR uncorrected and corrected measurements compared to the traditional tide gauge record. The errors in the phase-based corrected  $H_R$  are about half of those of the  $H_R$  without correction. The astronomic tide prediction from GNSS-IR performs better at predicting tide gauge water levels than the GNSS-IR estimates after correction (discrepancy of 7.26 cm with respect to tide gauge record). This means that non-astronomic variability is less than the remaining GNSS-IR errors after correction for this specific experiment. Even though the phase-based correction is calibrated over an interval when non-astronomic processes are absent, it can be used to correct  $H_R$  at any interval, including those when storm surge is significant and the prediction based on astronomic tides is inadequate. Figure 6d shows a comparison of the  $H_R$  with (black crosses) and without (red dots) the phase-based correction for 2 days. The blue curve represents the tide gauge record.

## 6. Measurements of GNSS-IR Significant Wave Height, $H_s$

As summarized by Alonso-Arroyo et al. (2014), the SNR interference pattern, expressed as oscillations, becomes weaker as elevation angle grows. Upon a certain elevation angle, the incoherent component of the SNR signal, associated with scattering at the sea surface, becomes dominant. The elevation angle at which the coherent and incoherent components become comparable,  $e_{co}$ , varies according to the sea surface roughness, which is assumed to be solely impacted by waves.

### 6.1. Method

The value of  $e_{co}$  is defined as the maximum angle at which reflection is coherent based on the criterion defined in Section 3.1. The Rayleigh criterion constitutes the simplest formulation to relate  $e_{co}$  to sea surface roughness. The Rayleigh criterion is expressed as,

$$\sigma_h = \frac{\lambda}{8\sin(e_{co})}, \quad (13)$$

where  $\sigma_h$  is the standard deviation of the sea surface elevation at the cut-off elevation angle,  $e_{co}$ . The factor 8 may change to 16 and 32 to define a more restrictive criterion (Alonso-Arroyo et al., 2014). Provided that sea

surface elevation follows a Gaussian distribution (and individual wave heights follow a Rayleigh distribution), the following relation holds between  $\sigma_h$  and the significant wave height,  $H_S$  (Alonso-Arroyo et al., 2014; Goda, 2010),

$$H_S \approx 4.004\sigma_h. \quad (14)$$

In situ wave measurements show that the factor 4.004 can also be as low as 3.8 (deep waters) (Goda, 2010). This criterion can be further improved by assuming the surface roughness is a homogeneous and stationary random field (Alonso-Arroyo et al., 2014) with a wavefield correlation length. It is noteworthy that these relations are expected to be invalid at the surf zone due to wave non-linearity (Goda, 2010).

Regardless of the model employed to relate  $H_S$  and  $e_{co}$ , the definition of  $e_{co}$  relies on the coherent reflection criterion of Equation 10 and the Rayleigh criterion of Equation 13, which in turn rely on arbitrary values (i.e.,  $\Omega_c$  in Equation 10 and the factor 8 in Equation 13). Given the ambiguity of determining the exact transition from coherent to incoherent reflections, we determine an empirical relation between  $\sin(e_{co})/\lambda$  and  $H_S$  obtained from a traditional instrumental wave gauge record. We include  $\lambda$  in the empirical relation because the three different constellations use slightly different wavelengths. After computing  $\sin(e_{co})/\lambda$  using Equation 13 for each satellite, the time series of  $\sin(e_{co})/\lambda$  estimates contains significant noise. This is efficiently removed by computing the median of each observation and their adjacent measurements within a 4 hr window.

The relation between the median  $\sin(e_{co})/\lambda$  and  $H_S$  is then calibrated with accurate measurements of  $H_S$ . We use the CDIP wave observations at the pier, described above. This record contains  $H_S$  values every hour, which are interpolated to estimate  $H_S$  at the same epoch as the GNSS-IR retrievals. Our methodology determines  $e_{co}$  with the coherent reflection criterion proposed in Section 3.1. We use  $\Omega_c = 0.33$ . Note this is a different value than that used for the  $H_R$ , where it is advantageous to cut off earlier than the exact transition. A sensitivity analysis is included in Supporting Information S1, where we determine that  $\Omega_c = 0.33$  maximizes the accuracy of the  $H_S$  estimates. We assume that wave properties do not change between the GNSS-IR footprints and the CDIP station, separated by less than 200 m (see Figure 2).

## 6.2. Resulting $H_S$ Measurements at E.B. Scripps Pier

Figure 7a presents a comparison between  $\sin(e_{co})/\lambda$  and the CDIP  $H_S$  record. We fit a power law to the data,

$$H_S = 0.1594(\sin(e_{co})/\lambda)^{-1.8224} + 0.2299, \quad (15)$$

with  $\lambda$  and  $H_S$  in meters. The curve decreases monotonically as  $e_{co}$  increases. Figures 7b and 7c present the estimated  $H_S$  values using the retrieved  $\sin(e_{co})/\lambda$  values and the power law. We observe good agreement with the wave gauge record for waves smaller than 1.8 m. Figures 7d and 7e show a comparison in which the error standard deviation is 0.12 m. This is similar to the accuracy achieved by Roggenbuck et al. (2019) using a different approach but similar reflection heights and minimum elevation angle. The accuracy is also comparable to other wave sensing technologies, such as in situ wave radars (Ewans et al., 2014) and satellite altimetry (Yang et al., 2020). There are two possible reasons why these experiments are able to measure higher waves than the maximum of 0.7 m from the experiment of Alonso-Arroyo et al. (2014). First, we analyze SNR oscillations for elevation angles as low as  $1^\circ$ , while Alonso-Arroyo et al. (2014) used a minimum elevation angle of  $5^\circ$ , which limits the range of wave heights they can measure. Second, we located the antenna  $\sim 10$  m over the sea surface while the previous experiment located the antenna  $\sim 3$  m over the sea surface (estimated from their deployment photographs). The higher the antenna, the higher the SNR oscillation frequency, and the better the resolution in the search for  $e_{co}$  described in Section 3.1. Our SNR records, however, fail to accurately estimate waves higher than 1.8 m for the greatest storms of November 2020 and January 2021, as shown in Figure 7c. We hypothesize that the expected  $e_{co}$  are smaller than the  $1^\circ$  minimum elevation angle analyzed in our experiment and, therefore, the method cannot estimate such high waves. Another alternative explanation is the occlusion caused by high waves which may reduce the reflecting signal strength. This effect can be illustrated with a picture of nearshore moonshine reflection, as shown in the supplemental material. High storm waves not only reduce the accuracy of  $H_S$ , but also of  $H_R$  as explained above. For high wave events we also expect that the number of observations will be reduced due to the lack of coherent reflections and occlusion.

## 6.3. $H_S$ Calibration

The method described above would be more useful for making measurements in remote areas if we could eliminate or reduce the time needed for calibration, such that a short temporary deployment of a pressure wave gauge

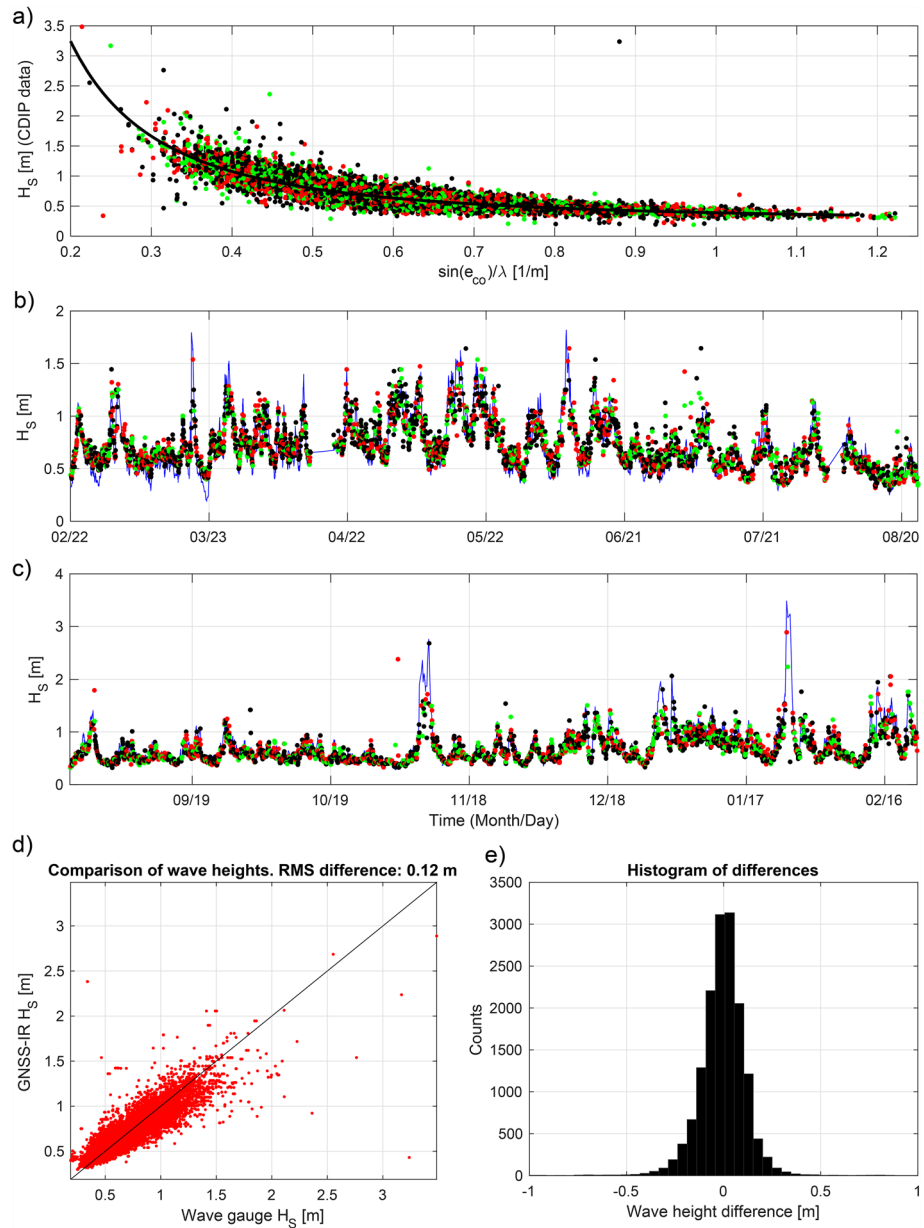


**Figure 7.** (a) Significant wave height record from a traditional wave gauge vs.  $e_{co}$ .  $e_{co}$  is defined as the transition elevation angle from coherent to incoherent reflection. The black line shows a fitted power law equal to  $H_s = 0.1594(\sin(e_{co})/\lambda)^{-1.8224} + 0.2299$ . Black, red and green dots represent observations from GPS, GLONASS and Galileo constellations, respectively. (b, c) Comparison between the wave gauge record (blue line) and the  $H_s$  estimates using the power law derived from (a). (d) Comparison of the GNSS-IR  $H_s$  estimate and the wave gauge. The standard deviation of the differences is 12.0 cm. (e) Histogram of the  $H_s$  differences between both records.

would suffice. We test the accuracy of GNSS-IR  $H_s$  retrievals as the calibration interval is reduced, and evaluate the prediction accuracy for the deployment period. Figure 8 columns a and b show the power law fit for different calibration intervals. Figures 8c and 8d show the prediction accuracy over the 1-year experiment. Calibration intervals as short as 1 day can achieve an RMS error of 15 cm, just slightly larger than using data from the entire experiment. However, when a short calibration period is used, errors are larger for high wave conditions, which are significantly reduced when calibration periods include storms.

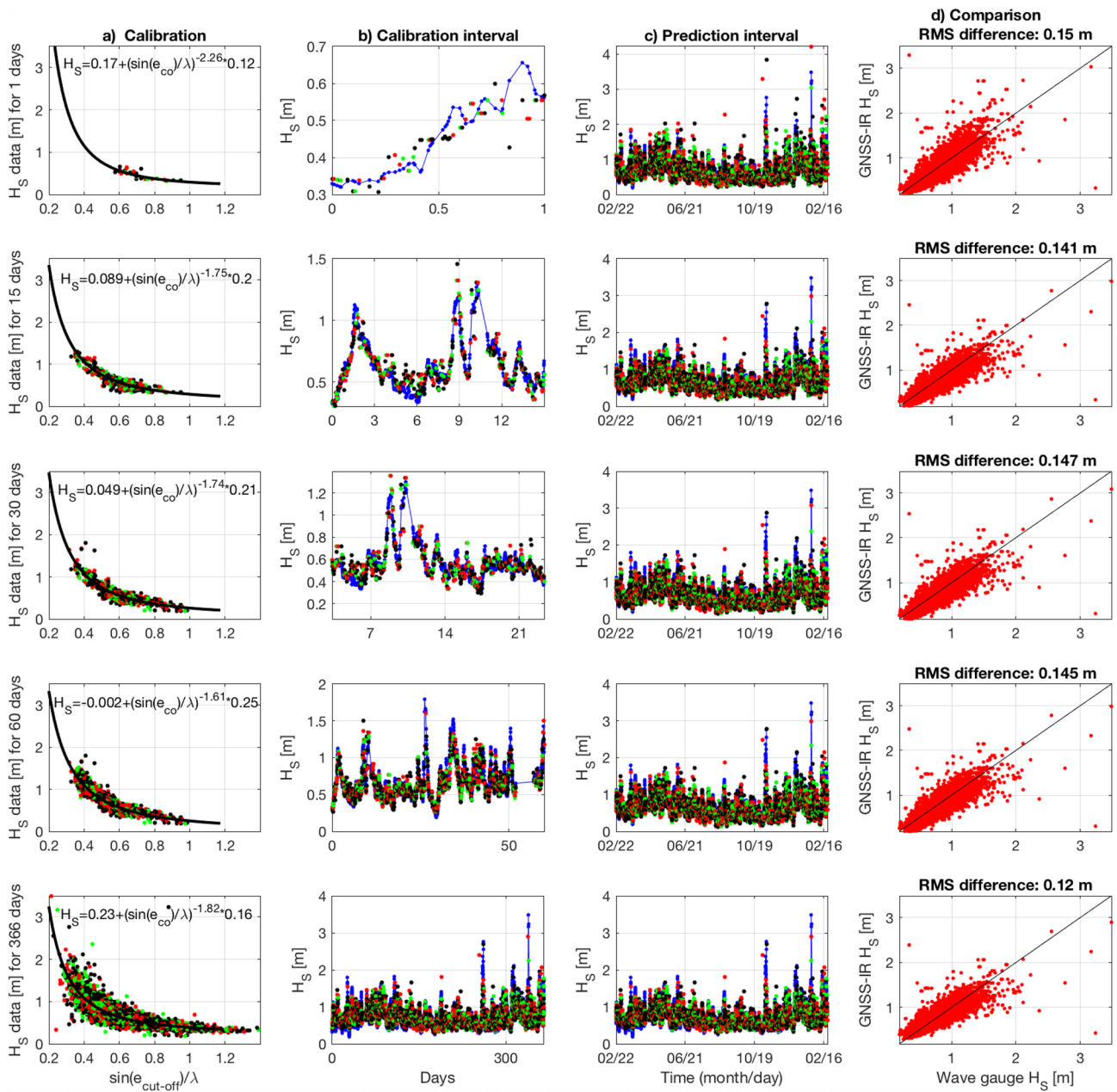


**Figure 8.** (a) Calibration of the power law relating  $H_S$  and  $\sin(e_{co})/\lambda$  for different time intervals. (b) Comparison of GNSS-IR and wave gauge  $H_S$  values over the calibration period. (c) Comparison of GNSS-IR and wave gauge  $H_S$  values over the 1-year deployment. The blue line represents the wave gauge data and the black, red and green dots represent observations from the GPS, GLONASS and Galileo constellations. (d) Scatter plot between the GNSS-IR and the wave gauge  $H_S$  values for the 1-year deployment. RMS differences are shown in the header for each calibration period.

## 7. Discussion

### 7.1. Potential Sources of Errors

The accuracy of  $H_R$  improves significantly with a phase-based correction, from an error standard deviation of 18.2–9.39 cm. This is a significant accuracy improvement but the final accuracy is still lower than the accuracy reported in some previous studies. We hypothesize that averaging and calculating a global fit over long periods, commonly used in other studies that report high accuracy, is one means to further reduce the high-frequency component of errors. However, we opt to avoid a global fit and treat each observation independently, so we maximize the effective temporal resolution of the record, and enable real-time applications of the measurements.



Furthermore, results from other locations may have other wave climatologies affecting the  $H_R$  accuracy. The  $H_R$  calculation shows that the largest errors have a correlation with high waves (i.e., wave heights over 2 m), even when the phase-based correction is applied. The presence of incoherent reflections at low elevation angles and wave occlusion may reduce the accuracy when determining peak frequencies and  $H_R$ . This constitutes a relevant limitation to the GNSS-IR method. It is worthwhile in the future to investigate the sensitivity of  $H_R$  accuracy to the wave conditions for different antenna heights. A higher antenna corresponds to more SNR oscillations in a narrow range of elevation angles and, possibly, a smaller impact of wave occlusion. Removing elevation angles lower than  $\sim 10^\circ$  (Henning, 2011), may be also inadequate for GNSS-IR under moderate to high wave conditions.

The astronomic tidal analysis demonstrates that accurate constituent amplitudes and phases can be determined at the pier, compared to those of a traditional tide gauge. This is possible because the errors in GNSS-IR  $H_R$  are non-stationary and of a short period. The high accuracy has been also quantified at other sites (e.g., Tabibi et al., 2020). The tidal coefficients determined from GNSS-IR have been shown to be useful for making phase-based corrections to  $H_R$  for determining more accurate water levels, even when non-astronomic processes such as storm surge are present.

The new simplified phase-based correction procedure, proposed in this study, removes the requirement for the use of a co-located tide gauge. The correction requires only a sufficiently long period of GNSS-IR measurements with low wave heights and low storm surge so the astronomic tide solely explains the water level variations. For most of the cases this is achieved with 1 month of measurements from which the commonly dominant tidal constituents M2 and S2 can be resolved. It would be useful to carry out the same experiments with a different deployment configuration to determine whether the functional form of the phase-based correction can be generalized.

Further analyses were carried out in Supporting Information S1 to identify the sources of  $H_R$  errors after phase-based correction. We analyzed error correlations with the  $H_R$  height-rate correction (Larson, Ray, et al., 2013; Larson et al., 2017), the significant wave height and the atmosphere refractivity. The height-rate correction (Equation S1 in Supporting Information S1) consists of an additional term in the standard  $H_R$  calculation (Section 3) and which becomes relevant for temporally varying  $H_R$ . We calculated the correction associated with the height-rate effect and compared it with phase-corrected  $H_R$  errors of Section 5, finding that they are uncorrelated. It is noteworthy that Tabibi et al. (2020) reported on the effect of the height-rate on the SNR phase. This suggests that the phase-based correction effectively compensates for the height-rate correction. Consistent with this, the correlation between the uncorrected  $H_R$  of Section 3 with the height-rate correction is significant (see Figure S3 in Supporting Information S1). The fact that the RMS is lower after applying the phase-based correction than after applying the height-rate correction from Equation 6 in Section 3 means that the phase-based correction is also compensating for additional unknown errors. Waves may also have an effect on  $H_R$ , even when they are low. While noisy, the scatter plot of errors versus significant wave height shows a trend in which larger errors are associated with higher waves. This is consistent with the explanation of Nievinski and Larson (2014a), stating that antennas only receive reflected signals from the wave crests, causing a systematic error. As for atmospheric effects, we first compared the  $H_R$  errors with refractivity (Haase et al., 2014) following the formulations of Rüeger (2002); Buck (1996). We did not observe a significant correlation. As a second analysis, we employed the ray-tracing techniques of Nikolaidou et al. (2020a, 2020b) to estimate a correction due to tropospheric delays. The correction is close to the absolute error of  $H_R$  obtained from a leveling with respect to geodetic reference points at the pier. Future research shall focus on these effects and include new methodologies (Nikolaidou et al., 2023).

For  $H_S$ , we could not remove the requirement for the use of a co-located wave gauge. The calibration period, though, may be as short as 1 day. High storm waves also reduce the accuracy of  $H_S$  and values over 1.8 m cannot be captured in our experiment. We attempted to improve the estimates of  $H_S$  by analyzing ranges with lower elevation angles. Lower elevation angles, however, introduce additional errors into the  $H_S$  and  $H_R$  estimates because of the additional delay of the signal traveling through the lower troposphere that contaminates the simple geometric height calculation. Indeed, we processed SNR time series with minimum elevation angles of  $0^\circ$ ,  $0.2^\circ$  and  $0.5^\circ$  and we could not gain better accuracy. Other sources of errors can also exist when determining the function  $H_S$  v/s  $e_{co}$ . The strength of reflected signals at the sea surface not only depends on the surface roughness but also on other aspects, such as the antenna gain pattern and whether the footprint of the reflecting material includes, for example, sand or rock on the coastline. While these effects are for the most part removed when de-trending the SNR raw signal, there may be still some remaining impact when determining  $e_{co}$ . Our experiment assumed that sea states are homogeneous between the wave gauge and the GNSS-IR  $H_S$  footprints ( $\sim 200$  m away). This

is reasonable in our case as depths are more than 12 m and the beach slope is  $\sim 4\%$  within the sensing region. This means that waves, with wavelengths on the order of 50 m, will not have a significant change in amplitude or wavelength on the seaward side (Mei et al., 2005). In our methodology, we also assumed that the homogeneous wavefield is represented by an isotropic random field. While this assumption seems to be reasonable in this experiment because of the good fit with wave gauge records, it may be not valid for experiments with longer waves and a well-defined propagation direction.

## 7.2. GNSS-IR Implementation Strategies

The experiment described here was carried out under optimal conditions with access to a high accuracy permanent tide gauge and wave gauge. The potential utility of the method, however, is to more easily capture data in remote areas without such infrastructure, and enable more sites to be deployed for establishing the wave and sea level climatologies in a wider range of environments. Given the calibration requirements, we propose the following workflow for new deployments to estimate  $H_R$  (with a phase-based correction) and  $H_S$  (with calibration). This workflow is applicable for antennas in the standard upright orientation, so the criteria may need to be modified for other types of antennas and orientations. We also recommend complementing this workflow with additional guidelines (e.g., Geremia-Nievinski & Hobiger, 2019) for assuring the proper exposure and siting for the clean reception of direct and reflected signals.

1. Deployment of the GNSS antenna in an area with the maximum field of view. Identify azimuthal ranges with a clear view to the sea surface. The elevation angle cut-off should allow recording down to  $1^\circ$ , and the sample interval should be 15 s or shorter. For existing geodetic stations, coordination with network operators should assure the additional quantity of data collected with a low elevation angle mask is within the data transmission specifications.
2. Short deployment of traditional wave gauge instrument for  $H_S$  calibration purposes. It is best to choose a time when moderate to high waves are likely, which would provide a better calibration. A single day is expected to be required to get 15 cm RMS for the wave height. The increase in accuracy of the 365 days calibration compared to 60 days was primarily due to including two large storms rather than due to the increase in length of the calibration period. This approach should be verified for other conditions.

The proposed data post-processing procedure over the initial calibration period is summarized below. We provide the following guidelines for estimating  $H_R$ .

1. Pre-select SNR time series with elevation angles as small as  $1^\circ$  and with a duration longer than 10 min. Only use data for elevation angles lower than  $30^\circ$ .
2. Determine the elevation angle cut-off,  $e_{co}$ , using the coherent reflection criterion in Equation 10. The value of  $\Omega_c$  determined in this study (i.e.,  $\Omega_c = 0.5$ ) can be adopted.
3. Remove the SNR oscillation decay  $e^{-D\sin^2(e)}$  of Equation 12 from the SNR time series, as explained in Section 5.1. Estimate  $H_R$  from the modified SNR time series using the standard procedure of Larson, Löfgren, and Haas (2013) and Equation 1.
4. Determine the amplitude and phase of the first seven astronomic tide constituents as demonstrated in the harmonic analysis of Section 3.2. Three months within the recorded data would be sufficient, optimally when wave heights are low. This can be refined as the length of the record increases. Reconstruct the astronomic tide for the GNSS deployment.
5. Calculate the non-astronomic residuals, equal to the  $H_R$  estimates minus the reconstructed astronomic tide, and low-pass filter to remove high frequency noise (i.e., the red curve in Figure 5f). Identify the time intervals when the low-pass filtered non-astronomic residuals are small.
6. Use the estimates of  $H_R$  for periods with small non-astronomic residuals to determine pseudo errors, defined as the  $H_R$  estimate minus the reconstructed astronomic tide.
7. Determine the SNR oscillation phase shift for each observation,  $\Phi_{snr}$ , using a Fourier expansion as described in Section 5.1. Plot  $\Phi_{snr}$  versus the pseudo-errors in the previous step. Fit a line and determine the slope, which will correspond to the phase-based correction, specific to the deployment. If necessary, remove points from the data set corresponding to phase shifts larger than  $\pi$  or smaller than  $-\pi$ , or correct them by  $\pi$  if it can be done without ambiguity.
8. Correct  $H_R$  obtained in step 2 to obtain the phase-based corrected  $H_R$ .
9. Optionally, the elevation angle cutoff criterion  $\Omega_c$  can be revisited and optimized. The difference between the  $H_R$  estimates and the tide-predicted  $H_R$  over a long time period could be used as a metric to be minimized.

Finally, we provide guidelines for estimating  $H_S$  as follows.

1. Pre-select SNR time series with elevation angles as small as  $1^\circ$  and with a duration longer than 10 min. Only use data for elevation angles lower than  $30^\circ$ .
2. Determine the elevation angle cut-off,  $e_{co}$ , using the coherent reflection criterion Equation 10 and  $\Omega_c = 0.33$ .
3. Using the temporary wave gauge measurements recorded over at least 1 day fit a curve of  $\sin(e_{co})/\lambda$  (where  $\lambda$  is the GNSS carrier signal wavelength) versus  $H_S$  measured with the wave gauge. We use a function with the form  $H_S = A \sin(e_{co})^B + C$ , where  $A$ ,  $B$  and  $C$  are the parameters to be fit.
4. Use  $e_{co}$  and the power law function of the previous step to compute  $H_S$  for the remainder of the GNSS deployment.
5. If the wave gauge can be deployed for a longer period and higher waves are recorded during that time, the value of  $\Omega_c$  and the power law function calibration can be revised.

## 8. Conclusions

For the particular conditions of this deployment in the high wave environment of the Pacific coast, the water level,  $H_R$ , is estimated with RMS errors of 9.4 cm, and significant wave height,  $H_S$ , is estimated with RMS better than 15 cm. The deployment setup of the experiment captures SNR signals from a broad range of azimuths, between  $200^\circ$  and  $330^\circ$ . The sea surface was sensed within a radius of  $\sim 600$  m from the pier. Implementing the technique for multi-GNSS constellations has resulted in more than doubling the average daily acquisitions to 42 irregularly spaced estimates of  $H_R$  and  $H_S$  per day. This resulted in temporal gaps of 56% of the experiment duration, compared to 77% for GPS only, with occasional gaps of up to 2 hr. This provides a promising lower accuracy alternative to a tide gauge for measuring water level variations with periods on the order of an hour and greater.

The accuracy of  $H_R$  and  $H_S$  are maximized by means of a criterion identifying coherent reflections. However, a correlation analysis shows that high waves are still a significant source of error. High waves reduce the range of elevation angles where reflections are coherent. Consequently, a shorter SNR time series must be used to estimate  $H_R$  and errors increase. Maximizing the antenna height could potentially compensate for that by providing more cycles of SNR variation over the lowest elevation angles and by reducing the impact of wave occlusion.

The accuracy of  $H_R$  is further maximized by means of a phase-based correction which uses the astronomic tide prediction. This correction reduces the errors by about 50%. The  $H_R$  with phase-based correction is useful, for example, when attempting to measure storm surge. It would be particularly useful in inland or sheltered waters, and less so offshore, where high waves often accompany storm surge, affecting the accuracy and number of  $H_R$  observations.

While the sensitivity of GNSS-IR to wave state is an issue in the  $H_R$  retrievals, it is a valuable property used to estimate significant wave height in moderate conditions. The  $H_S$  estimates achieve a reasonable accuracy using a calibration over a very short interval, on the order of 1 day. Thus, the nearly optimal GNSS-IR accuracy could be achieved with a short and relatively inexpensive temporary deployment of a traditional bottom pressure wave gauge added to the GNSS deployment effort. The method appears to reach saturation for  $H_S$  higher than 1.8 m, although further work with different antenna heights should investigate the possibility to increase this limit.

The sensing characteristics will be different for other experiment geometries, yielding a different temporal resolution and sensed area. Maximizing the azimuthal field of view is desirable. Optimization of the antenna height in particular should be explored in future work because it could improve the accuracy of both  $H_R$  and  $H_S$ . While SNR time series with lower elevation angles are desirable, the corresponding signals are potentially more affected by atmospheric delays due to the longer path through the lower troposphere. In this work, we do not observe a correlation between  $H_R$  errors and changes in the refractivity but they may impact the accuracy of absolute water level measurements. The feasibility of a general function relating  $H_S$  and  $e_{co}$  that would be applicable for any antenna height should also be investigated to determine whether the calibration period could be eliminated.

GNSS-IR constitutes an attractive technique to enlarge the global data set of coastal sea state observations due to the relatively low deployment and operational costs. The support of new smartphones to raw GNSS measurements (e.g., Android-based devices) can also make GNSS-IR accessible to more users. However, these advantages must be balanced against the lower accuracy of retrieved water levels and significant wave height relative to traditional instruments. The GNSS-IR technique can serve in a variety of coastal environments where other technologies

cannot measure. For example, GNSS antennas can be deployed in isolated regions where supporting marine structures such as piers and wharves for traditional instruments are absent. GNSS-IR deployments could also be useful for measuring extreme events, such as hurricanes and tropical storms, as antennas can be deployed at a safe distance from the water. The wavefield constitutes a critical parameter when evaluating the accuracy of GNSS-IR coastal observations for this purpose. Although the significant wave height estimation method saturates for waves higher than 1.8 m, this may be sufficient for monitoring wave conditions within port harbors, which is essential for safe operations.

## Data Availability Statement

Coastal water level and meteorological data were retrieved from NOAA's website for the LAJO stations (<https://tidesandcurrents.noaa.gov/waterlevels.html?id=9410230>), which are publicly available. The wave data was retrieved from CDIP's website for the Scripps Pier station (<https://cdip.ucsd.edu/themes/?p=b=1&d2=p70&u2=s:073:st:1:v:parameter>), which is publicly available. Ephemerides of GNSS satellites (SP3 files) were retrieved from NASA Archive of Space Geodesy Data. ([https://doi.org/10.5067/GNSS/GNSS\\_IGSMGEXP\\_001](https://doi.org/10.5067/GNSS/GNSS_IGSMGEXP_001)) (IGS, 2012). Data is publicly available but users need to have a free account in NASA Earth-data. Sp3 files are organized by week. RINEX files are generated using teqc code, available at <https://www.unavco.org/software/data-processing/teqc/teqc.html> (Estey & Meertens, 1999). Rinex files are available at <https://doi.org/10.5281/zenodo.7971822> (Sepúlveda et al., 2023a). SNR data files are generated using codes developed by Carolyn Roesler and Kristine M. Larson, available at <https://github.com/kristinemlarson/gnssSNR> (Roesler & Larson, 2018). Positioning GNSS files of the antenna for DOY 53 and 242 in 2020 are included in the Supporting Information S1 and they are also available at <https://doi.org/10.5281/zenodo.7909120> (Sepúlveda et al., 2023b).

## Acknowledgments

We acknowledge P. Hudson for exploratory work on the pier deployment. We acknowledge the insightful discussions with K. Larson, F. Geremia-Nievinsky, S. Williams, and M.A. Karegar about GNSS-IR advances, T. Nikolaidou for helping us to test the atmospheric correction in our experiment and D. Caccamise for providing information about geodetic benchmarks close to our deployment. We thank the anonymous peer-reviewers who provided a thorough review of the manuscript and provided insightful comments. I. Sepúlveda would like to acknowledge the support of the John Miles Fellowship and the Green Foundation during the execution of this project and the San Diego State University SEED grant. Support was also provided by National Aeronautics and Space Administration Grant NNX15AU19G and National Science Foundation Grants 1835372 and 1642650.

## References

- Alonso-Arroyo, A., Camps, A., Park, H., Pascual, D., Onrubia, R., & Martín, F. (2014). Retrieval of significant wave height and mean sea surface level using the GNSS-R interference pattern technique: Results from a three-month field campaign. *IEEE Transactions on Geoscience and Remote Sensing*, 53(6), 3198–3209. <https://doi.org/10.1109/tgrs.2014.2371540>
- Anderson, K. D. (2000). Determination of water level and tides using interferometric observations of GPS signals. *Journal of Atmospheric and Oceanic Technology*, 17(8), 1118–1127. [https://doi.org/10.1175/1520-0426\(2000\)017<1118:dowlat>2.0.co;2](https://doi.org/10.1175/1520-0426(2000)017<1118:dowlat>2.0.co;2)
- Behrens, J., Terrill, E., & Thomas, J. (2018). CDIP wave observations during hurricanes Irma, Jose, and Maria, and a nor'easter. *Shore and Beach*, 86(3), 14–20.
- Bernier, N. B., & Thompson, K. R. (2015). Deterministic and ensemble storm surge prediction for Atlantic Canada with lead times of hours to ten days. *Ocean Modelling*, 86, 114–127. <https://doi.org/10.1016/j.ocemod.2014.12.002>
- Buck, A. L. (1996). *Buck research CR-1A user's manual*. Buck Research Instruments.
- Burcharth, H. F., & Hughes, S. (2000). *Coastal engineering manual, fundamentals of design, chapter 5, part VI. to be published by coastal engineering research center, waterways experiment station*. US Army Corps of Engineers.
- Codiga, D. L. (2011). *Unified tidal analysis and prediction using the UTide Matlab functions*. Graduate School of Oceanography, University of Rhode Island Narragansett.
- Estey, L. H., & Meertens, C. M. (1999). TEQC: The multi-purpose toolkit for GPS/GLONASS data. *GPS Solutions*, 3(1), 42–49. <https://doi.org/10.1007/pl00012778>
- Ewans, K., Feld, G., & Jonathan, P. (2014). On wave radar measurement. *Ocean Dynamics*, 64(9), 1281–1303. <https://doi.org/10.1007/s10236-014-0742-5>
- Georgiadou, Y., & Kleusberg, A. (1988). On carrier signal multipath effects in relative GPS positioning. *Manuscripta Geodaetica*, 13(3), 172–179.
- Geremia-Nievinsky, F., & Hobiger, T. (2019). Site guidelines for multi-purpose GNSS reflectometry stations.
- Geremia-Nievinsky, F., Hobiger, T., Haas, R., Liu, W., Strandberg, J., Tabibi, S., et al. (2020). SNR-based GNSS reflectometry for coastal sea-level altimetry: Results from the first IAG inter-comparison campaign. *Journal of Geodesy*, 94(8), 1–15. <https://doi.org/10.1007/s00190-020-01387-3>
- Goda, K. (2015). Effects of seabed surface rupture versus buried rupture on tsunami wave modeling: A case study for the 2011 Tohoku, Japan, earthquake. *Bulletin of the Seismological Society of America*, 105(5), 2563–2571. <https://doi.org/10.1785/0120150091>
- Goda, Y. (2010). *Random seas and design of maritime structures* (Vol. 33). World Scientific Publishing Company.
- Godin, G. (1970). The resolution of tidal constituents. *International Hydrographic Review*.
- Haase, J. S., Murphy, B. J., Muradyan, P., Nievinsky, F. G., Larson, K. M., Garrison, J. L., & Wang, K.-N. (2014). First results from an airborne GPS radio occultation system for atmospheric profiling. *Geophysical Research Letters*, 41(5), 1759–1765. <https://doi.org/10.1002/2013gl058681>
- Henning, W. (2011). User guidelines for single base real time GNSS positioning.
- International GNSS Service (IGS). (2012). GNSS IGS multi-GNSS experiment (MGEX) product [Dataset]. NASA Crustal Dynamics Data Information System. [https://doi.org/10.5067/GNSS/GNSS\\_IGSMGEXP\\_001](https://doi.org/10.5067/GNSS/GNSS_IGSMGEXP_001)
- Janssen, P. A. E. M., & Bidlot, J.-R. (2018). Progress in operational wave forecasting. *Procedia IUTAM*, 26, 14–29. <https://doi.org/10.1016/j.piutam.2018.03.003>
- Kang, H., Chun, I., & Oh, B. (2020). New procedure for determining equivalent deep-water wave height and design wave heights under irregular wave conditions. *International Journal of Naval Architecture and Ocean Engineering*, 12, 168–177. <https://doi.org/10.1016/j.ijnaoe.2019.09.002>
- Kennedy, A. B., Gravois, U., Zachry, B., Luettich, R., Whipple, T., Weaver, R., et al. (2010). Rapidly installed temporary gauging for hurricane waves and surge, and application to hurricane Gustav. *Continental Shelf Research*, 30(16), 1743–1752. <https://doi.org/10.1016/j.csr.2010.07.013>



- Larson, K. M., Löfgren, J. S., & Haas, R. (2013a). Coastal sea level measurements using a single geodetic GPS receiver. *Advances in Space Research*, 51(8), 1301–1310. <https://doi.org/10.1016/j.asr.2012.04.017>
- Larson, K. M., Ray, R. D., Nievinski, F. G., & Freymueller, J. T. (2013b). The accidental tide gauge: A GPS reflection case study from Kachemak Bay, Alaska. *IEEE Geoscience and Remote Sensing Letters*, 10(5), 1200–1204. <https://doi.org/10.1109/lgrs.2012.2236075>
- Larson, K. M., Ray, R. D., & Williams, S. D. P. (2017). A 10-year comparison of water levels measured with a geodetic GPS receiver versus a conventional tide gauge. *Journal of Atmospheric and Oceanic Technology*, 34(2), 295–307. <https://doi.org/10.1175/jtech-d-16-0101.1>
- Larson, K. M., Small, E. E., Gutmann, E., Bilich, A., Axelrad, P., & Braun, J. (2008). Using GPS multipath to measure soil moisture fluctuations: Initial results. *GPS Solutions*, 12(3), 173–177. <https://doi.org/10.1007/s10291-007-0076-6>
- Larson, K. M., Small, E. E., Gutmann, E. D., Bilich, A. L., Braun, J. J., & Zavorotny, V. U. (2008). Use of GPS receivers as a soil moisture network for water cycle studies. *Geophysical Research Letters*, 35(24), L24405. <https://doi.org/10.1029/2008gl036013>
- Liu, W., Beckheinh, J., Semmling, M., Ramatschi, M., Vey, S., Wickert, J., et al. (2017). Coastal sea-level measurements based on GNSS-R phase altimetry: A case study at the Onsala space observatory, Sweden. *IEEE Transactions on Geoscience and Remote Sensing*, 55(10), 5625–5636. <https://doi.org/10.1109/tgrs.2017.2711012>
- Löfgren, J. S., Haas, R., & Scherneck, H.-G. (2014). Sea level time series and ocean tide analysis from multipath signals at five GPS sites in different parts of the world. *Journal of Geodynamics*, 80, 66–80. <https://doi.org/10.1016/j.jog.2014.02.012>
- Löfgren, J. S., Haas, R., Scherneck, H.-G., & Bos, M. S. (2011). Three months of local sea level derived from reflected GNSS signals. *Radio Science*, 46(06), 1–12. <https://doi.org/10.1029/2011rs004693>
- Lomb, N. R. (1976). Least-squares frequency analysis of unequally spaced data. *Astrophysics and Space Science*, 39(2), 447–462. <https://doi.org/10.1007/bf00648343>
- Mei, C. C., Stiassnie, M., & Yue, D. K.-P. (2005). *Theory and applications of ocean surface waves: Linear aspects* (Vol. 23). World Scientific.
- Nievinski, F. G., & Larson, K. M. (2014a). Forward modeling of GPS multipath for near-surface reflectometry and positioning applications. *GPS Solutions*, 18(2), 309–322. <https://doi.org/10.1007/s10291-013-0331-y>
- Nievinski, F. G., & Larson, K. M. (2014b). Inverse modeling of GPS multipath for snow depth estimation—Part I: Formulation and simulations. *IEEE Transactions on Geoscience and Remote Sensing*, 52(10), 6555–6563. <https://doi.org/10.1109/tgrs.2013.2297681>
- Nikolaidou, T., Santos, M., Williams, S., & Geremia-Nievinski, F. (2023). Development and validation of comprehensive closed formulas for atmospheric delay and altimetry correction in ground-based GNSS-R. *IEEE Transactions on Geoscience and Remote Sensing*, 61, 1–7. <https://doi.org/10.1109/tgrs.2023.3260243>
- Nikolaidou, T., Santos, M., Williams, S. D. P., & Geremia-Nievinski, F. (2020a). A simplification of rigorous atmospheric raytracing based on judicious rectilinear paths for near-surface GNSS reflectometry. *Earth Planets and Space*, 72(1), 1–10. <https://doi.org/10.1186/s40623-020-01206-1>
- Nikolaidou, T., Santos, M. C., Williams, S. D. P., & Geremia-Nievinski, F. (2020b). Raytracing atmospheric delays in ground-based GNSS reflectometry. *Journal of Geodesy*, 94(8), 68. (submitted). <https://doi.org/10.1007/s00190-020-01390-8>
- Park, J., Heitsenrether, R., & Sweet, W. (2014). Water level and wave height estimates at NOAA tide stations from acoustic and microwave sensors. *Journal of Atmospheric and Oceanic Technology*, 31(10), 2294–2308. <https://doi.org/10.1175/jtech-d-14-00021.1>
- Peng, D., Hill, E. M., Li, L., Switzer, A. D., & Larson, K. M. (2019). Application of GNSS interferometric reflectometry for detecting storm surges. *GPS Solutions*, 23(2), 47. <https://doi.org/10.1007/s10291-019-0838-y>
- Portner, H. O., Roberts, D. C., Masson-Delmotte, V., Zhai, P., Tignor, M., Poloczanska, E., et al. (2019). IPCC, 2019: IPCC special report on the ocean and cryosphere in a changing climate.
- Press, W. H., Teukolsky, S. A., Flannery, B. P., & Vetterling, W. T. (1992). *Numerical recipes in Fortran 77: Volume 1, of Fortran numerical recipes: The art of scientific computing*. Cambridge University Press.
- Puente, V., & Valdés, M. (2019). Sea level determination in the Spanish coast using GNSS-R. In *Multidisciplinary digital publishing institute proceedings* (Vol. 19, p. 11).
- Pugh, D. T. (1987). Tides, surges and mean sea level.
- Purnell, D., Gomez, N., Chan, N. H., Strandberg, J., Holland, D. M., & Hobiger, T. (2020). Quantifying the uncertainty in ground-based GNSS-reflectometry sea level measurements. *IEEE Journal of Selected Topics in Applied Earth Observations and Remote Sensing*, 13, 4419–4428. <https://doi.org/10.1109/jstars.2020.3010413>
- Roesler, C., & Larson, K. M. (2018). Software tools for GNSS interferometric reflectometry (GNSS-IR). *GPS Solutions*, 22(3), 80. <https://doi.org/10.1007/s10291-018-0744-8>
- Roggenbuck, O., Reinking, J., & Lambertus, T. (2019). Determination of significant wave heights using damping coefficients of attenuated GNSS SNR data from static and kinematic observations. *Remote Sensing*, 11(4), 409. <https://doi.org/10.3390/rs11040409>
- Rüeger, J. M. (2002). Refractive index formulae for electronic distance measurement with radio and millimetre waves. *UNISURV Rep*, 68.
- Scargle, J. D. (1982). Studies in astronomical time series analysis. II-statistical aspects of spectral analysis of unevenly spaced data. *The Astrophysical Journal*, 263, 835–853. <https://doi.org/10.1086/160554>
- Sepúlveda, I., Cao, B., Haase, J. S., & Murphy, M. (2023a). Compact RINEX dataset of: Optimizing simultaneous water level and wave measurements from multi-GNSS interferometric reflectometry over one year at an exposed coastal site. [Dataset]. Zenodo. <https://doi.org/10.5281/zenodo.7971822>
- Sepúlveda, I., Cao, B., Haase, J. S., & Murphy, M. (2023b). Positioning GNSS data of optimizing simultaneous water level and wave measurements from multi-GNSS interferometric reflectometry over one year at an exposed coastal site. [Dataset]. Zenodo. <https://doi.org/10.5281/ZENODO.7909120>
- Sepúlveda, I., Liu, P. L.-F., Grigoriu, M., Haase, J. S., & Winckler, P. (2022). Non-stationary probabilistic tsunami hazard assessments compound-ing tides and sea level rise. *Earth's Future*, 10(11), e2022EF002965. <https://doi.org/10.1029/2022ef002965>
- Sepúlveda, I., Liu, P. L.-F., Grigoriu, M., & Pritchard, M. (2017). Tsunami hazard assessments with consideration of uncertain earthquake slip distribution and location. *Journal of Geophysical Research: Solid Earth*, 122(9), 7252–7271. <https://doi.org/10.1002/2017jb014430>
- Soulat, F., Caparrini, M., Germain, O., Lopez-Dekker, P., Taani, M., & Ruffini, G. (2004). Sea state monitoring using coastal GNSS-R. *Geophysical Research Letters*, 31(21). <https://doi.org/10.1029/2004gl020680>
- Strandberg, J. (2020). New methods and applications for interferometric GNSS reflectometry.
- Strandberg, J., Hobiger, T., & Haas, R. (2016). Improving GNSS-R sea level determination through inverse modeling of snr data. *Radio Science*, 51(8), 1286–1296. <https://doi.org/10.1002/2016rs006057>
- Strandberg, J., Hobiger, T., & Haas, R. (2019). Real-time sea-level monitoring using Kalman filtering of GNSS-R data. *GPS Solutions*, 23(3), 61. <https://doi.org/10.1007/s10291-019-0851-1>
- Tabibi, S., Geremia-Nievinski, F., Francis, O., & van Dam, T. (2020). Tidal analysis of GNSS reflectometry applied for coastal sea level sensing in Antarctica and Greenland. *Remote Sensing of Environment*, 248, 111959. <https://doi.org/10.1016/j.rse.2020.111959>



- Tabibi, S., Geremia-Nievinski, F., & van Dam, T. (2017). Statistical comparison and combination of GPS, GLONASS, and multi-GNSS multipath reflectometry applied to snow depth retrieval. *IEEE Transactions on Geoscience and Remote Sensing*, 55(7), 3773–3785. <https://doi.org/10.1109/tgrs.2017.2679899>
- Wang, X., He, X., & Zhang, Q. (2020). Coherent superposition of multi-GNSS wavelet analysis periodogram for sea-level retrieval in GNSS multipath reflectometry. *Advances in Space Research*, 65(7), 1781–1788. <https://doi.org/10.1016/j.asr.2019.12.023>
- Wang, X., Zhang, Q., & Zhang, S. (2019). Sea level estimation from SNR data of geodetic receivers using wavelet analysis. *GPS Solutions*, 23(1), 6. <https://doi.org/10.1007/s10291-018-0798-7>
- Williams, S., & Nievinski, F. (2017). Tropospheric delays in ground-based GNSS multipath reflectometry—Experimental evidence from coastal sites. *Journal of Geophysical Research: Solid Earth*, 122(3), 2310–2327. <https://doi.org/10.1002/2016jb013612>
- Winckler, P., Sepúlveda, I., Aron, F., & Contreras-López, M. (2017). How do tides and tsunamis interact in a highly energetic channel? The case of Canal Chacao, Chile. *Journal of Geophysical Research: Oceans*, 122(12), 9605–9624. <https://doi.org/10.1002/2017jc012680>
- Xin, W., Qiang, S., XunXie, Z., DaRen, L., LianJun, S., Xiong, H., et al. (2008). First China ocean reflection experiment using coastal GNSS-R. *Chinese Science Bulletin*, 53(7), 1117–1120. <https://doi.org/10.1007/s11434-008-0110-2>
- Yang, J., Zhang, J., Jia, Y., Fan, C., & Cui, W. (2020). Validation of Sentinel-3a/3b and Jason-3 altimeter wind speeds and significant wave heights using buoy and ASCAT data. *Remote Sensing*, 12(13), 2079. <https://doi.org/10.3390/rs12132079>
- Zheng, N., Chen, P., Li, Z., Ma, Y., & Liu, L. (2020). Tide height inversion and accuracy analysis based on GNSS-MR technology. In *China satellite navigation conference* (pp. 141–152). Springer.